Build Simul (2023) 16: 889–913
https://doi.org/10.1007/s12273-022-0971-3

# Quantifying spatiotemporal variability in occupant exposure to an indoor airborne contaminant with an uncertain source location

**John E. Castellini Jr.[1], Cary A. Faulkner[1], Wangda Zuo[2,3] (✉), Michael D. Sohn[4]**

*1. Department of Mechanical Engineering, University of Colorado Boulder, UCB 427, Boulder, CO 80309, USA*
*2. Department Architectural Engineering, The Pennsylvania State University, University Park, PA 16802, USA*
*3. National Renewable Energy National Laboratory, Golden, CO 80401, USA*
*4. Energy Analysis and Environmental Impacts Division, Lawrence Berkeley National Laboratory, 1 Cyclotron Road, Berkeley, CA 94720, USA*

## Abstract

Well-mixed zone models are often employed to compute indoor air quality and occupant exposures. While effective, a potential downside to assuming instantaneous, perfect mixing is underpredicting exposures to high intermittent concentrations within a room. When such cases are of concern, more spatially resolved models, like computational-fluid dynamics methods, are used for some or all of the zones. But, these models have higher computational costs and require more input information. A preferred compromise would be to continue with a multi-zone modeling approach for all rooms, but with a better assessment of the spatial variability within a room. To do so, we present a quantitative method for estimating a room's spatiotemporal variability, based on influential room parameters. Our proposed method disaggregates variability into the variability in a room's average concentration, and the spatial variability within the room relative to that average. This enables a detailed assessment of how variability in particular room parameters impacts the uncertain occupant exposures. To demonstrate the utility of this method, we simulate contaminant dispersion for a variety of possible source locations. We compute breathing-zone exposure during the releasing (source is active) and decaying (source is removed) periods. Using CFD methods, we found after a 30 minutes release the average standard deviation in the spatial distribution of exposure was approximately 28% of the source average exposure, whereas variability in the different average exposures was lower, only 10% of the total average. We also find that although uncertainty in the source location leads to variability in the average magnitude of transient exposure, it does not have a particularly large influence on the spatial distribution during the decaying period, or on the average contaminant removal rate. By systematically characterizing a room's average concentration, its variability, and the spatial variability within the room important insights can be gained as to how much uncertainty is introduced into occupant exposure predictions by assuming a uniform in-room contaminant concentration. We discuss how the results of these characterizations can improve our understanding of the uncertainty in occupant exposures relative to well-mixed models.

## Keywords

uncertainty;
variability;
airborne contaminant;
spatiotemporal variability;
well-mixed;
heterogeneity

## Article History

Received: 24 August 2022
Revised: 10 November 2022
Accepted: 28 November 2022







## 1 Introduction

Well-mixed multi-zone airflow models are commonly used to predict contaminant transport in indoor settings and predict occupant exposures to airborne contaminants. These models decompose a building into a series of zones, each assumed to have instantaneous perfect mixing. They are especially efficient in simulating large spatial-scale problems. For example, they have been used to assess contaminant transport scenarios in settings ranging from a

E-mail: wangda.zuo@psu.edu

## List of symbols

*General notation*

| | |
|---|---|
| $C$ | concentration (conc.) [kg/m$^3$] |
| $\mathcal{C}$ | massless concentration [m$^{-3}$] |
| $E$ | exposure (exp.) [s·kg/m$^3$] |
| $\mathcal{E}$ | massless exposure [s/m$^3$] |
| $t$ | time/time from start of release [s] |
| $t_{avg}$ | averaging time [s] |
| $t_d$ | time from end of release [s] |
| $t_{mix}$ | mixing time [s] |
| $t_{rel}$ | releasing time [s] |
| $\mathcal{T}$ | temporary time-integration variable |
| $\overline{X}$ | arithmetic mean of a set $X$ |
| $\tilde{X}$ | variable/uncertain value of $X$ |

*Subscripts*

| | |
|---|---|
| D | decaying period |
| fit | parameter from curve fit |
| $i$ | measuring location index |
| $j$ | source location index |
| R | releasing period |
| WM | well-mixed (WM) model |
| $^*$ | mean-normalized quantity |

*Room parameters*

| | |
|---|---|
| $G$ | contaminant generation rate [kg/s] |
| $V$ | room volume [m$^3$] |
| $Q$ | volume flow rate [m$^3$/s] |
| $C_{in}$ | supply air conc. [kg/m$^3$] |
| $C(t)$ | WM room conc. [kg/m$^3$] |

*Well-mixed model parameters*

| | |
|---|---|
| $C_{0,WM}$ | WM initial conc. [kg/m$^3$] |
| $C_{D,WM}$ | decaying period WM conc. [kg/m$^3$] |
| $C_{R,WM}$ | releasing period WM conc. [kg/m$^3$] |
| $C_{SS,WM}$ | WM steady-state conc. [kg/m$^3$] |
| $E_{R,WM}$ | releasing period WM exp. [kg/m$^3$] |
| $E_{D,WM}$ | decaying period WM exp. [kg/m$^3$] |
| $\tau_{WM}$ | WM room time constant [s] |

*Variability metrics*

| | |
|---|---|
| $s_X$ | sample standard deviation in set $X$ |
| $s_X^2$ | sample standard variance in set $X$ |
| $\delta_X$ | general measure of variability in $X$ |
| $\delta_X^*$ | normalized variability in $X$ |

*Average metrics*

| | |
|---|---|
| $\mathcal{C}_{ij} \equiv \mathcal{C}_j(t,\vec{x}_i)$ | conc. of source-$j$ at point $\vec{x}_i$ |
| $\overline{\mathcal{C}}_j$ | source-averaged conc. of source-$j$ |
| $\overline{\overline{\mathcal{C}}}_j$ | total-average concentration |
| $\mathcal{E}_{ij} \equiv \mathcal{E}_j(t,\vec{x}_i)$ | exp. to source-$j$ at point $\vec{x}_i$ |
| $\overline{\mathcal{E}}_j$ | source-averaged exp. to source-$j$ |
| $\overline{\overline{\mathcal{E}}}_j$ | total-average exposure |

*Curve fit parameters*

| | |
|---|---|
| $\mathcal{C}_{0,fit}$ | decaying period initial fit conc. |
| $\mathcal{C}_{0,CFD}$ | decaying period CFD initial conc. |
| $\mathcal{C}_{D,fit}(t_d)$ | decaying period fitted avg. conc. |
| $\mathcal{C}_{R,fit}(t)$ | releasing period fitted avg. conc. |
| $\mathcal{C}_{SS,fit}$ | releasing period scaling term |
| $\mathcal{C}_{SS,fit^*}$ | steady-state conc. |
| $\mathcal{C}_{I,D,fit}$ | decaying period mixing-stage offset |
| $\mathcal{C}_{I,R,fit}$ | releasing period mixing-stage offset |
| $\tau_{R,fit}$ | releasing period time constant |
| $\tau_{D,fit}$ | decaying period time constant |

wing or floor of a building (Faulkner et al. 2022a, 2022b; Ma et al. 2022), to an entire building (Li et al. 2005; Lim et al. 2010), or city and regional scale analyses (Shrubsole et al. 2012; Jones et al. 2015; Shi et al. 2015; Lu et al. 2020; Molina et al. 2021). Similarly, well-mixed models can also efficiently assess long temporal-scale problems, such as simulations of contaminant concentrations over the course of a year. And they have been widely shown to provide good estimations of average transient indoor contaminant concentrations in many situations.

While well-mixed approaches are well-suited and practical for many applications, they have some potential downsides. For example, they may underpredict occupant exposures by not capturing areas of high intermittent contaminant concentrations within a zone, or room. The heterogeneity in the distribution of contaminants within a room can be caused by a myriad of in-room conditions (e.g. source locations, ventilation strategies, temperature gradients). More spatially resolved approaches, such as computational fluid dynamics (CFD) methods, are often applied to address these scenario-specific concerns. Their ability to model the influence of complex airflow patterns on airborne contaminant transport has been studied in both experimental (Jayaraman et al. 2006; Zhang et al. 2007; Yin et al. 2009; Barbosa and de Carvalho Lobo Brum 2021; Fu et al. 2022) and real-world settings (Ho 2021), for a variety of enclosed

spaces. Studies have applied CFD methods to investigate spatial distributions of contaminants in medical settings (Méndez et al. 2008; Qian et al. 2009; King et al. 2013; Hang et al. 2015; Bhattacharyya et al. 2020), on public transportation (Zhu et al. 2012; Li et al. 2016; Yan et al. 2017; Yang et al. 2020), in classrooms (Abuhegazy et al. 2020; Ascione et al. 2021; Mirzaie et al. 2021), at restaurants (Chitaru et al. 2018; Ho 2021), and in different office settings (Lee et al. 2009; Kong et al. 2015; Barbosa and de Carvalho Lobo Brum 2021; Castellini et al. 2022), often with the aim of understanding the influence of particular boundary conditions on in-room contaminant distributions. However, the added model fidelity of these methods increases the computational burden and information needed, making them impractical for some applications (Morozova et al. 2020). An ideal compromise would be to continue to use multi-zone approaches, but with a better assessment of the spatial and temporal (i.e. spatiotemporal) variability of concentrations and occupant exposure that goes beyond the well-mixed assumption.

A recent review of the state of airborne contaminant modeling (Bueno de Mesquita et al. 2022) noted the investigation of spatial heterogeneity within rooms and the quantification of its impact on exposure predictions as key research priorities in the field of airborne infectious disease modeling requiring further exploration. Another review (Dias and Tchepel 2018) of personal exposure to contaminants in urban environments concluded that the spatiotemporal dynamics of contaminant transport can vary greatly based on the specific exposure scenario, and the authors call for strategies to quantitatively compare trends in variability in different scenarios.

In this paper we take the first steps towards developing the desired intermediate models to predict the uncertain spatiotemporal distribution of possible exposures occupants may see in a given room, while also helping to fill the gaps noted in Bueno de Mesquita et al. (2022) and Dias and Tchepel (2018), with the ultimate aim of incorporating these uncertain-room models into a multi-zone modeling framework. Here we present a method for systematically quantifying the levels of spatiotemporal variability in the distributions of a generic airborne contaminant within a room. We develop a series of performance metrics to quantify the spatiotemporal variability in the contaminant concentration, and demonstrate the application of these metrics using a simplified case of an empty room with a single uncertain input condition, the location of the source within the room. Though the proposed methodology could be used to quantify the spatiotemporal variability in scenarios defined by any number of uncertain inputs, provided that spatially- and temporally-dense measurements of concentration are available for a representative sample of instances of the uncertain space. The metrics developed in this study enable the quantitative comparison of spatiotemporal trends in a wide range of scenarios, like those listed above, and meet the need noted by Dias and Tchepel (2018). The method enables the characterization of the impact that uncertainty in specific room parameters has on the temporal development of the contaminant distributions within the space. We first assess and quantify the variability in the average transient concentrations for the set of observed instances, while vary particular parameter(s) of interest, e.g. the source location. We then apply a regression curve fit to characterize the transient behavior of each case with a set of characteristic *fit*-parameters and evaluate how the transient contaminant profile varies in the sample as a result of the uncertain experimental variable(s). The level of variability in the spatial distribution of concentration is then quantified relative to the observed transient average in each instance, to distinguish between variability in the total magnitude and variability in space. Finally, we evaluate the total spatiotemporal variability in concentration for a given situation, quantifying the impact of uncertainty in the examined input room parameters on the total variability in possible local exposures and comparing these results to the well-mixed prediction.

Using a validated CFD model, we generated a spatially and temporally dense set of concentration measurements for each sample source location. Studies, such as Castellini et al. (2022) and Singer et al. (2022), have shown that the location of a source within a room and how it interacts with the room airflow greatly influences the pattern and level of heterogeneity in a room's contaminant distribution. For this reason, we focus on the source location as the uncertain variable of interest in this case study, and note that it is often a primary concern for indoor hazard assessments. We simulate a pseudo-random sample of 50 possible source locations, discuss the trends we observe during both the releasing and decaying periods of the concentration time series, and then draw conclusions about the relationship between uncertainty in the source location and the level of spatiotemporal variability in occupant exposures we expect in this room. Finally, we compare the CFD predictions to those from a well-mixed model to draw insight into the expected discrepancies in occupant exposures.

The remainder of this paper is organized as follows. First, we discuss the standard mass balance for a single well-mixed zone and derive an equation for the well-mixed transient concentration. We then describe the CFD model used in this study to calculate the spatially resolved transient concentrations, including a discussion of the model validation. Next, we present the novel method for quantifying spatiotemporal uncertainty in more detail. And then describe the room examined in our case study, as well as the set of

possible point source locations which define our experimental space. We then present the results of the case study in detail, applying our proposed method to characterize the spatiotemporal variability in this room, and assess the impact of source location uncertainty on spatially-resolved predictions of uncertain local exposures. Finally, we summarize some of the major findings from this study and highlight several potential future applications for this method.

## 2 Background

In this section, we first discuss typical well-mixed models used in multi-zone building simulations. We present the derivation of the well-mixed models from a single-zone mass balance and discuss some of the simplifying assumptions made in this work in the interest of modeling a generic contaminant. We then discuss the CFD model used in this study to capture the spatially resolved transient concentrations used as our uncertain data set in this study.

### 2.1 Well-mixed model

Well-mixed contaminant transport models often divide a building into multiple zones (typically, a zone contains one or more rooms). In each zone, the average transient concentration, $C(t)$ [kg/m$^3$], is assumed to be uniform and is calculated using a contaminant mass balance of the following form:

$$\frac{dC(t)}{dt} = \overbrace{\left[G(t) + QC_{in}(t)\right]/V}^{g(t)} - C(t)\overbrace{\left[Q/V + \lambda\right]}^{r} \quad (1)$$

where $V$ [m$^3$] is the volume of the room, $G$ [kg/s] is the internal contaminant generation rate in the space, $Q$ [m$^3$/s] is the room ventilation rate, and $C_{in}$ [kg/m$^3$] is the concentration of contaminants in the air being supplied to the room. In a multi-zone context, $Q$ and $C_{in}$ can be decomposed further to represent transport between multiple rooms. However, this paper focuses on contaminant transport in a single room with one inlet and one outlet. The parameter $\lambda$ [s$^{-1}$] represents a series of contaminant-dependent decay rates such as the virus inactivation rate, or the expected deposition rate of a given contaminant. The term $g(t)$ [(kg/s)/m$^3$], on the right hand side of Eq. (1), represents the room's total volumetric generation rate, while the term $r$ [s$^{-1}$] represents the total contaminant removal rate of the room.

To focus on the transient dispersion of an arbitrary contaminant located within our room of interest, we make several convenient assumptions to modify Eq. (1). First, we assume that no contaminants are being introduced by outside supply airflow ($C_{in} = 0$). Here, we will consider the case of a constant source with an arbitrary strength $G$, which results in a simplified volumetric generation rate $g(t) = G/V$. Second, we neglect the deposition and decay of the airborne contaminant ($\lambda = 0$). For fine aerosolized particles (< 3 μm) and contaminants that decay slowly (i.e. $\lambda \ll Q/V$), these rates are small relative to the removal of contaminants through mechanical ventilation. Similar studies have also made this simplifying assumption (i.e. $\lambda = 0$, or $r = Q/V$) when simulating contaminant transport in enclosed spaces (Zhu et al. 2012; Hang et al. 2015; Li et al. 2016; Ai et al. 2020b; ElDegwy et al. 2020; Barbosa and de Carvalho Lobo Brum 2021; Castellini et al. 2022) and others have experimentally confirmed that trace-gases, which exhibit no decay or deposit, are a suitable analog for fine aerosol particles (Yin et al. 2009; Ai et al. 2020a, 2020b). When not assessing specific in-room interventions designed to increase these rates (e.g. deposition onto barriers (Abuhegazy et al. 2020; Ren et al. 2021) or UV germicidal irradiation (Kanaan 2019; Buchan et al. 2020; Hou et al. 2021)) the overall effect of variability in these quantities on uncertainty in occupant exposure predictions can be examined more efficiently using well-mixed models, such as in Liao et al. (2005) and Jones et al. (2021).

We can divide the family of solutions to Eq. (1) into periods based on the source strength, (1) the *releasing period* and (2) the *decaying period*. During the releasing period, the source strength is a constant rate $G$. During the decaying period, there is no source release and the indoor contaminant concentration decays from its peak concentration. Solutions to Eq. (1) are shown in Eq. (2) and Eq. (3), respectively.

$$C_{R,WM}(t) = \frac{g}{r}\left(1 - e^{-tr}\right) = C_{SS,WM}\left(1 - e^{-t/\tau_{WM}}\right), \quad \text{if } t \le t_{rel} \quad (2)$$

$$C_{D,WM}(t_d) = \left[C_{R,WM}(t_{rel})\right]e^{-t_d r} = C_{0,WM}e^{-t_d/\tau_{WM}}, \quad \text{if } t_d \ge 0 \quad (3)$$

Several key parameters describing the transient behavior of the room are represented in Eqs. (2) and (3). The room time constant, $\tau_{WM}$ [s], represents the inverse of the contaminant removal rate in a well-mixed room. When a room is observed to have a time constant higher than the well-mixed model, its contaminant removal rate is lower. This leads to faster build-up/slower removal of contaminants than well-mixed models predict. In Eq. (2), $C_{SS,WM}$ [kg/m$^3$] is the steady-state contaminant-concentration that the room will reach as $t \to \infty$ for a constant, continuous contaminant release, and is equal to the ratio of contaminant generation and removal rates in the room. Here $t$ [s] is the time from the start of the release. In Eq. (3), $t_d$ [s] indicates the time from the start of the decaying period, after a finite source of duration $t_{rel}$, $t_d = t - t_{rel}$. Equation (3) also assumes that the

initial decay-period concentration, $C_{0,WM}$ [kg/m$^3$], is given by the concentration at the end of some finite releasing period, $C_{0,WM} = C_{R,WM}(t_{rel})$.

The exposure for an occupant in a well-mixed room is the time-integrated concentration in the room, stated in the units of [s·kg/m$^3$]. The duration of the exposure period, $t_a - t_b$, is thus expressed as Eq. (4), and Eq. (5), where $\mathcal{T}$ is simply a dummy variable used in integration:

$$E_{R,WM}(t) = \int_0^t C_{R,WM}(\mathcal{T})\mathrm{d}\mathcal{T} \tag{4}$$

$$E_{D,WM}(t_d) = \int_0^{t_d} C_{D,WM}(\mathcal{T})\mathrm{d}\mathcal{T} \tag{5}$$

## 2.2 Computational fluid dynamics model

This study uses CFD to calculate the spatially-resolved transient concentrations (ANSYS® Fluent 2021 R2, ANSYS 2021). We used a steady-state RNG $k$-$\varepsilon$ model to simulate the turbulent airflow in this space. Zhang et al. (2007) and Zhai et al. (2007) compared several turbulence models and demonstrated the capability of this type of model to predict airflows and contaminant dispersion in a variety of enclosed spaces with forced ventilation, and it has since been widely applied and validated in a variety of indoor environments. A Boussinesq approximation was used to solve for the effects of buoyant forces on the flow field and link the energy equation to the Reynolds-Averaged Navier-Stokes (RANS) airflow model. Radiation effects were ignored because of the relatively small temperature differences in our designed case, described in Section 4.

We used a Lagrangian particle-track model because it has been demonstrated to be more efficient in simulating the transient dispersion of a contaminant when the airflow field is steady (Zhang and Chen 2007). In the interest of evaluating trends for a generic contaminant and enabling a more broad interpretation and application of our results, we employ a massless contaminant transport model in this study. This model ignores thermal, inertial, and gravitational effects on the simulated contaminant trajectories, calculating them based only on the local steady-state airflow field. This simplification also enables the easy scaling of the reported results based on different source strengths. The impact of turbulence on the trajectories is simulated using a discrete random walk (DRW) model (ANSYS 2021) at each Lagrangian particle time-step. We also ignore diffusive forces and any particle-particle interactions because we are simulating a sparse contaminant.

The above assertions represent the transport of a neutrally buoyant trace gas contaminant. There are a variety of gaseous contaminants that can be found in indoor environments (WHO 2010). And previous studies have shown both experimentally (Yin et al. 2009; Ai et al. 2020a, 2020b) and numerically (Zhu et al. 2012; Hang et al. 2015; Li et al. 2016; ElDegwy et al. 2020; Ai et al. 2020b; Barbosa and de Carvalho Lobo Brum 2021) that tracer gases can also serve as a suitable surrogate for the transport of fine particulate contaminants as well, such as PM2.5 or smaller virus-laden respiratory aerosols, in enclosed ventilated spaces.

# 3 Methods

In this section, we propose a method for systematically evaluating the spatiotemporal variability of contaminants within enclosed spaces (Figure 1). We first discuss the utility of developing our model using source normalized

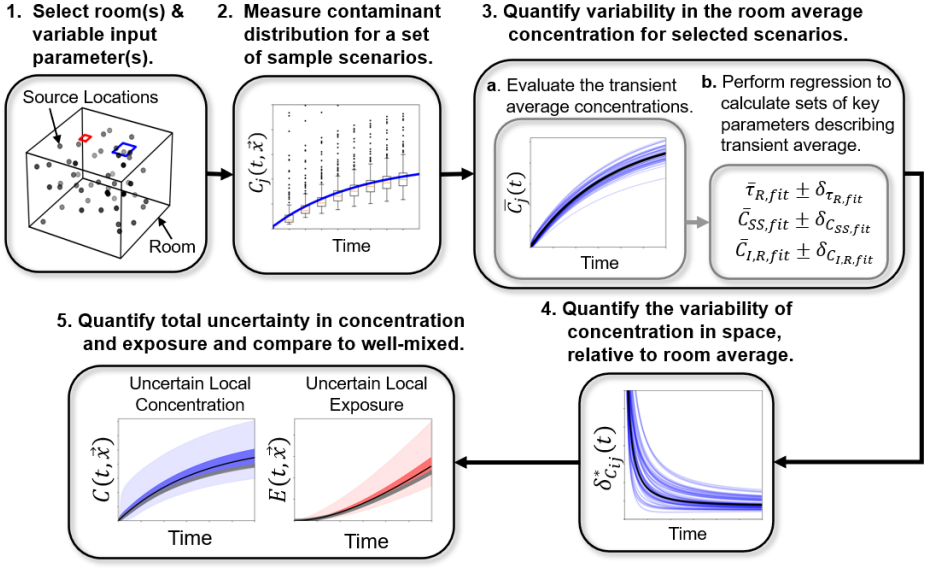


**Fig. 1** Methodology for assessing the spatiotemporal variability in indoor contaminant distributions presented in this study

massless measures of concentration. We then present the regression-based curve fit model used to characterize the trends in the average transient concentration and present the notation used to discuss variability in the spatial distribution of contaminants and different aspects of the room's average behavior. We then present additional detail on the methods used to accelerate the Lagrangian contaminant transport model used to generate the spatially resolved concentration data in this study and present the results of the simulations used to validate these methods.

### 3.1 Massless concentration and exposure

The subscript $i$ refers to a measurement at a location in space, $\vec{x}_i = (x_i, y_i, z_i)$ [m]. The subscript $j$ refers to some instance of the uncertain scenario being modeled, here it refers measurements corresponding to some source location $\vec{x}_j = (x_j, y_j, z_j)$ [m]. The concentration from source $j$ measured at a particular point, $\vec{x}_i$, and time $t$, is written as $C_{ij}(t)$. In this study, we present values of concentration normalized by the mass of contaminants released by the source over an arbitrary time period. Here we use $\Delta t$ = 0.5 s, as the sampling and integration time-step. Equation (6) shows an example of this normalization:

$$\mathcal{C} = \frac{C}{G\Delta t} \tag{6}$$

where $\mathcal{C}$ represents the mass normalized concentration in units of [m$^{-3}$], used for the remainder of this paper. Our discussion of exposure is also presented in a mass normalized form, using $\mathcal{E}$ to denote a mass normalized measure of exposure in units of [s/m$^3$], which is equal to an integral of $\mathcal{C}$ over some exposure period:

$$\mathcal{E}(t) = \int_0^t \mathcal{C}(\mathcal{T})\mathrm{d}\mathcal{T} \tag{7}$$

We chose to develop our model in terms of an arbitrary massless contaminant for several reasons. Firstly, this enables the results of our arbitrary contaminant model to quickly be scaled based on the generation rate of some particular contaminant of interest, such as the quanta generation of some particular virus. The model we develop here to describe the transient behavior of a room with an arbitrary massless contaminant source of constant strength, $G$, and releasing duration, $t_{\mathrm{rel}}$, can be extended to describe a similar source with a transiently varying strength, $G(t)$. Consider, any transient releasing function $G(t)$ could be discretized into a linear combination of $k$ constant strength finite duration releases described by our proposed model. Because we are dealing with sparse contaminants (i.e., mass diffusivity is negligible), we can similarly use linear combinations of our models' outputs (i.e., the uncertain concentration/exposure), scaled by some strength $G_k$ and duration $t_{\mathrm{rel,k}}$, to predict the uncertain transient concentration for any releasing function $G(t)$. However, for brevity, we will limit our discussion in this work to releases of constant, arbitrary strength, $G$.

### 3.2 Measures of average concentration and exposure

We define the *source average* concentration or exposure as the average concentration or exposure from a particular source, $j$, at all $n_{\mathrm{pts}}$ breathing zone measuring points, $i$ as:

$$\bar{\mathcal{C}}_j(t) = \frac{1}{n_{\mathrm{pts}}}\sum_{i=1}^{n_{\mathrm{pts}}} \mathcal{C}_{ij}(t) \tag{8}$$

$$\bar{\mathcal{E}}_j(t) = \frac{1}{n_{\mathrm{pts}}}\sum_{i=1}^{n_{\mathrm{pts}}} \mathcal{E}_{ij}(t) \tag{9}$$

Next, we define the *total average* concentration or exposure as the average of all the source average concentrations or exposure from all of the $n_{\mathrm{s}}$ scenarios considered, which in the example that follows is the set of source average concentrations from the $n_{\mathrm{s}}$ = 50 different source locations considered:

$$\bar{\bar{\mathcal{C}}}_j(t) = \frac{1}{n_{\mathrm{s}}}\sum_{j=1}^{n_{\mathrm{s}}} \bar{\mathcal{C}}_j(t) \tag{10}$$

$$\bar{\bar{\mathcal{E}}}_j(t) = \frac{1}{n_{\mathrm{s}}}\sum_{j=1}^{n_{\mathrm{s}}} \bar{\mathcal{E}}_j(t) \tag{11}$$

### 3.3 Curve fitting of the source-average concentrations

To consider the time-varying trends in a room's average concentration, we develop a regression model to fit the transient change in the room's source average concentration. The model allows us to assess the specific ways in which particular uncertain input parameters influence the variability in the room's transient average concentration. To better understand how $\bar{\mathcal{C}}_j(t)$ differs from the well-mixed model for different source locations we used a least-squares regression technique to estimate the parameters in Eq. (12), for the releasing, and Eq. (13), for the decaying periods, both based on the form of the well-mixed model, Eqs. (2) and (3) respectively.

$$\bar{\mathcal{C}}_{\mathrm{R,fit}}(t) = \mathcal{C}_{\mathrm{SS,fit}}(1 - \mathrm{e}^{-t/\tau_{\mathrm{R,fit}}}) + \mathcal{C}_{\mathrm{I,R,fit}} \tag{12}$$

$$\bar{\mathcal{C}}_{\mathrm{D,fit}}(t_{\mathrm{d}}) = \mathcal{C}_{0,\mathrm{fit}} \cdot \mathrm{e}^{-t_{\mathrm{d}}/\tau_{\mathrm{D,fit}}} \tag{13}$$

where $\tau_{\mathrm{R,fit}}$ and $\tau_{\mathrm{D,fit}}$ [s] are the observed room time-constants calculated for the releasing and decaying periods respectively,

$\mathcal{C}_{SS,fit}$ and $\mathcal{C}_{0,fit}$ are scaling terms, and $\mathcal{C}_{I,R,fit}$ is a linear intercept term, all in the units of (massless) concentration [$m^{-3}$]; while $\overline{\mathcal{C}}_{R,fit}$ and $\overline{\mathcal{C}}_{D,fit}$ are the transient room average concentrations predicted by the proposed curve fitting model for the two periods.

For the most part, these *fit*-parameters have similar physical meanings to the *WM*-parameters discussed in Section 2.1. For example, $\tau_{R,fit}$ and $\tau_{D,fit}$ have the same physical meaning as $\tau_{WM}$ in Eqs. (2) and (3). The only significant difference was the addition of an intercept term, $\mathcal{C}_{I,R,fit}$, in Eq. (12). We introduced it in order to better account for and quantify the initial shift in the behavior of the average concentration during the mixing stage, the initial portion of each period before the observed source average curve begins to follow the smooth curves predicted by Eqs. (12) and (13). The source average curves do not follow a predictable path during this stage, and for this room and air flow rate, the duration of the initial mixing stage tends to be fairly short, $t_{mix} < 120$ s, and so we focus in this paper on characterizing the variability outside this period. As a result of including a non-zero intercept, the steady-state concentration predicted by this model equivalent to the well-mixed term, $\mathcal{C}_{SS,WM}$, is slightly different and can be written as $\mathcal{C}_{SS,fit^*} = \mathcal{C}_{SS,fit} + \mathcal{C}_{I,R,fit}$.

For the decaying period, $\mathcal{C}_{0,fit}$ represents the initial concentration we would expect at $t_d = 0$, based on the behavior of the average concentration after the mixing stage. This is approximately equivalent to $\mathcal{C}_{0,WM}$ in Eq. (3). However $\mathcal{C}_{0,fit}$ will typically differ from the actual concentration observed at the start of the decaying period in CFD, denoted $\mathcal{C}_{0,CFD} = \overline{\mathcal{C}}_j(t_d = 0)$. This is due to a similar initial shift in the behavior of the source average concentration during the decaying period's mixing stage, just after the source is stopped. To help quantify this decay-period mixing stage shift, we define an additional term, $\mathcal{C}_{I,D,fit} = \mathcal{C}_{0,CFD} - \mathcal{C}_{0,fit}$, as the difference between the observed CFD initial value and that predicted by the curve fit. This is roughly equivalent to the $\mathcal{C}_{I,R,fit}$ term in the releasing period.

### 3.4 Measuring variability

The proposed methodology will facilitate the assessment of several aspects of a room's spatiotemporal variability; variability in the source average, variability in space, and the combined total variability. Steps 3–5 in Figure 1. We use the notation $\delta_X$ to represent a measurement of variability in some set of observed quantities $X$. In this study, we assume Gaussian statistics for all the variabilities discussed and use the sample standard deviation $s_X = \delta_X$, for discussing variability in different quantities. It is defined as the square root of the sample variance $s_X^2$, shown in Eq. (14) for a sample of size $N$:

$$s_X^2 = \frac{\sum (X_i - \overline{X})^2}{N-1} \tag{14}$$

We examine the variability in a variety of different data sets using the metrics described above including the transient variability in the set of average concentrations ($\delta_{\overline{\mathcal{C}}_j}(t)$), as well as the variability in the sets of fit parameters ($\delta_{\mathcal{C}_{SS,WM}}$, etc.), and the total variability of concentration in space ($\delta_{\mathcal{C}_{ij}}(t)$). To better compare the amount of variability in these data sets, we normalize the measured variabilities by the mean of the corresponding set, $\overline{X}$, giving a standard dimensionless measure of variability denoted as $\delta_X^* = \delta_X / \overline{X}$, which can be discussed in the units of [% of $\overline{X}$]. And finally, as a shorthand representation of an uncertain (varying) parameter we will use the following notation:

$$\widetilde{X} \equiv \overline{X} \pm \delta_X \tag{15}$$

where $\widetilde{X}$ is a probability distribution of possible values for a parameter $X$, with $\overline{X}$ and $\delta_X$ representing its known or observed mean and variability for a specified situation. Each component of Eq. (15) may vary with time and may also be dependent on other known or uncertain room parameters. The proposed method enables the investigation of these trends in time and the interactions between different room parameters and the uncertainty in exposure predictions for different cases.

### 3.5 Accelerating the Lagrangian transport model

In this study, we employed two methods, described in Chen et al. (2015), for accelerating the Lagrangian simulations by reducing the number of particle trajectories required to explain the trends in the contaminant transport within a room. The first technique leverages the steady-state nature of the flow field and employs the principle of linear *superimposition*. The transient trajectories of an instantaneous release of $N_{par}$ Lagrangian particles can be superimposed a number of times, $n_{super}$ with each successive superimposition shifted in time by some time step, $\Delta t$ [s]. This can effectively simulate a constant source of strength $G = N_{par}/\Delta t$ and duration $n_{super}\Delta t$, but calculating only $1/n_{super}$ the number of trajectories one would need to simulate when not using superimposition in order to have a similarly sufficient number of Lagrangian particles.

The other technique described in Chen et al. (2015) was the use of *time-averaging*, or taking a centered rolling average of the transient concentration. This smooths the high-frequency fluctuations in local measures of concentration that are caused by having too few Lagrangian particles in

the simulation, resulting in local concentrations changing dramatically from one time step to the next. When these fluctuations are large relative to the instantaneous local concentration, it introduces an additional local measurement uncertainty, which would confound our efforts to accurately measure the instantaneous spatial variability in our set of monitoring points. Time averaging allows us to reduce this measurement uncertainty without simulating additional trajectories, which would also reduce the relative magnitude of the fluctuations but simultaneously would increase the computational time, which is roughly proportional to the number of trajectories simulated.

### 3.6 Validation and verification of CFD methods

For this work, we verified that the poly-hexcore mesh settings used in these simulations provided a mesh-independent solution of the airflow field in our validation case, shown in Figure 2(a). Many studies, including Castellini et al. (2022), have validated the steady-state RNG $k$-$\varepsilon$ RANS model used in this study by comparing predicted and experimentally measured airflow data in a variety of environments. We compared traces of the steady-state temperature and velocity fields at multiple points in the room for three meshes of increasing density. Each mesh had surface refinements at inlets and outlets and used boundary-layer cells at each wall, with max cell lengths of 0.1, 0.2, and 0.3 m respectively. The middle set of mesh settings (max length 0.2 m) was found to be sufficiently fine to resolve the airflow field and provide a mesh-independent solution.

To validate our transient contaminant transport model, we used experimental data from a study by Fu et al. (2022). Figure 2(a) shows the set-up of the experimental chamber in this study. The test chamber was an empty room with a side-wall mixing ventilation setup; it has two inlets near the top of the room, and a single outlet on the lower portion of the same wall. The ventilation rate was approximately 5.6 air changes per hour (ACH). Under steady-state airflow conditions, a tracer-gas, 1% $SF_6$ solution, was released at a constant rate (0.2 L/min) from a 3 cm spherical point-source for a release duration of $t_{rel}$ = 10 s.

While measurements of local flow velocities were unavailable for this case, this data set included two sets of concentration measurements at multiple points in space. The measurements from the quartz-enhanced photoacoustic spectroscopy (QEPAS) sensor provide a highly time-resolved data set for the concentration, and these QEPAS measurements agree well with the more prevalent Brüel and Kjær (B&K) sampling system. The local concentrations from CFD were calculated using a user-defined-function (UDF) inFluent which counted the number of Lagrangian particles within a spherical measuring volume, $V_{meas}$ = 0.015 m$^3$, centered about each measuring point. Figure 2(b) shows that the prediction of our CFD model matches fairly well with the experimentally measured local concentrations at several points in the room. The result verifies that this modeling methodology is able to capture the major trends in transient contaminant dispersion within this and similar rooms.

## 4 Case description

In the interest of focusing our discussion on our proposed methodology for characterizing a room's spatiotemporal variability, we evaluate a relatively simple case in this study

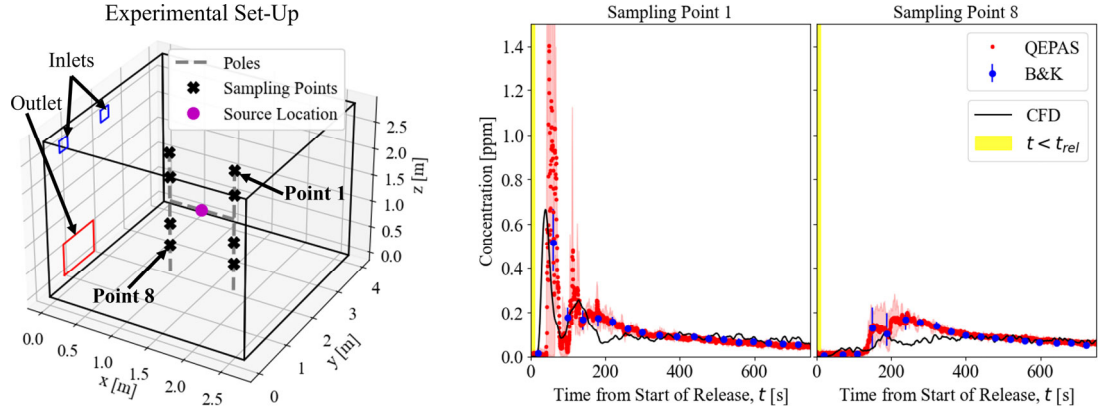


(a) Diagram of experimental chamber

(b) Validation results at two points

**Fig. 2** (a) Schematic of the experimental chamber set-up used in Fu et al. (2022) with the source location (purple) and the eight sampling points (black), as well as the airflow inlets (blue) and outlet (red). (b) shows a comparison of the experimentally measured transient tracer gas concentration from the two measurement systems used in the experiment, the QEPAS (red) and B&K (blue), as well as the CFD-measured concentration (black), shown for a $t_{rel}$ = 10 s point-source release measured at two of the sampling locations denoted in (a)

with only a single uncertain input condition, the location of a source within a room. We will discuss in Sections 6.1 and 8 how this process can be extended to evaluate more detailed scenarios and applied to evaluate trends in a room's uncertain performance for a higher-dimensional uncertain space, i.e. considering a larger number of uncertain boundary conditions.

Here we investigate the trends in an empty, rectangular office room 4.3 × 3.0 × 3.2 [m] (14 × 10 × 10.5 [ft]), depicted in Figure 3. This room is similar in many ways to the validation case discussed previously. It has a mixing ventilation system with an eight-way-throw 0.3 m (1 ft) square inlet diffuser, modeled using the momentum inlet method described in Srebric and Chen (2002), with an inlet angle of 30° relative to ceiling plane. The airflow outlet was a single 0.6 m (2 ft) square HVAC return diffuser also located on the ceiling. A uniform surface heat flux of 28 W/m$^2$ was applied to the floor to simulate a total room heat load of 361 W. This is meant to represent some arbitrary arrangement of heat sources within a hypothetical one or two-person office. In a real room, the thermal plumes created by local heat sources (e.g. occupants, electronics) would create different local flow patterns that would influence the contaminant transport (Ivanov and Mijorski 2019; Sun et al. 2021). While this case ignores these geometry-specific impacts, our arbitrary floor heat source enables us to capture the added buoyant mixing effect (Baughman et al. 1994) that might be expected in a real office. We simulated a variable air volume system operating in a cooling condition with an air exchange rate of 3.7 ACH (43 L/s or 91 cfm) and a supply air temperature of 14 °C and a room set-point

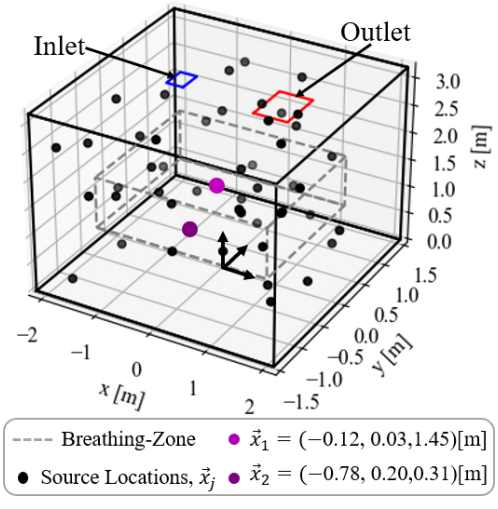


**Fig. 3** Diagram of the investigated room showing the dimensions, locations of the airflow inlet (blue) and outlet (red), the monitored room breathing zone (grey), and the locations of the point sources used in the multidimensionally uniform Latin-Hypercube sample (black). The two source locations used as examples in Section 5.2 are also highlighted (purple/pink)

of 20 °C. Using the same set of mesh controls as in our validation case, we also performed a mesh independence study for this room generating meshes of 110,241, 234,753, and 1,102,459 cells. As in our validation case, we found that the 234,753 cell mesh provided a mesh-independent representation of the flow field in our case study room.

The unknown input condition we focus on in this study is the uncertain location of an arbitrary contaminant within this room. We define the experimental space of possible source locations as the entire volume of the room, i.e, black lines in Figure 3. We used the algorithm presented in Deutsch and Deutsch (2012) to generate a 50-point multi-dimensionally uniform Latin Hypercube sample of this space, shown as the points in Figure 3, which we assume to be representative of the population of possible source locations. For each source location, we simulated an instantaneous point-release of $N_{par}$ = 29,685 particles and tracked their trajectories over a 30-minute simulation period. Using the method of superimposition (Chen et al. 2015), discussed in Section 3.5, we then constructed our data sets for sources of different durations ranging from 15 s to a continuous release for each location. By developing our model based on point releases of massless contaminants, we can use the concept of superimposition again (this time in space instead of time) to approximate an arbitrary source of any size/shape within the experimental space we investigated (e.g., a gaseous release from a surface, or a combination of multiple sources). Consider, a release of any shape/size within this domain could be thought of as some combination of point releases within the uncertain space represented by our simulated sample, therefore, assuming the sample is truly representative of our scenario of interest, the user needs only consider the magnitude of the uncertain contaminant release within the room, as we discussed in Section 3.1. Alternatively, if we sought to construct a model for a specific type of sources, such as an exhaled pathogen or a surface release of some gaseous contaminant, we would change the sample space of sources we simulated accordingly, by limiting the release locations to where occupants are likely to be or to the surface(s) releasing contaminants. Constraining the possible source location in this way would likely reduce the associated spatiotemporal uncertainty in a given case and result in different *fit*-parameter distributions.

As with the possible source location, the possible location of a room's occupants, i.e. the region we wish to model, may be known to some greater or lesser degree and taken into account in the design of the CFD experiment. For example, if we know how occupants tend to use a given space we could define some three-dimensional probability density function, $p(x_i, y_i, z_i) = w_i$ where $w_i$ represents the likely hood of a occupant being located at some measuring

point $\vec{x}_i = [x_i, y_i, z_i]$. In this example arbitrary example case we measured the transient concentration from each release at two sets of measuring points $\vec{x}_i$. The first was a set of 964 points distributed throughout the entire domain. And the second set was constrained to the region of the room where occupants are likely to breath-in an airborne contaminant. This set of $n_{pts}$ = 448 uniformly-spaced measuring points located within the room's *breathing-zone*, defined based on ASHRAE's definition of 0.6 m (2 ft) from each wall and between 0.9–1.8 m (3–6 ft) above the floor (ASHRAE 2019), will be the focus of this study. Because have no additional information as to how the occupants are likely to use this space arbitrary space, we applied a uniform weighting function, $w_i = 1/n_{pts}$, to our set of measuring points. In the remainder of this paper, all discussions of variability, and all figures (excepting Figure 12) will refer only to this second set of occupied breathing zone measuring points. Comparisons of differences in the observed variability for the two different sets of monitoring points were omitted for brevity.

## 5 Results

We start with a brief discussion of the airflow field in the room. Next, the contaminant distribution from two example source locations are shown to discuss some of the general trends in the transient behavior of the spatial distribution of contaminants in this room. We then discuss in detail the observed variability in the breathing zone source averages for the full set of 50 source locations. We then analyze the trends of variability in space about these averages, and finally discuss the combined total variability in the range of expected concentrations and exposure in this room when the contaminant source's location is unknown.

### 5.1 Room airflow

The paths taken by contaminants away from particular source locations are highly dependent on the airflow in the room. Differences in local airflow velocities explain the variability in both the average concentration computed from different source locations and the spatial variability of concentration within the room. For example, when a source is located in a region with higher than average local flow velocity, the contaminants tend to disperse more quickly than when the source is located in a region with low flow velocity. Similarly, if the source is located near the outlet or where the airflow is moving directly towards an outlet, they are removed from the room at a significantly faster rate compared to sources in regions of low velocity, or within a local recirculation zones. Figure 4 shows the velocity vector field at the mid-plane of this room, $y$ = 0, as well as the location of the two example sources. Both of these sources were located fairly close to this mid-plane and are shown projected onto it to give a sense of the flow near these releasing locations which we will discuss in more detail in the following section. We can see at the mid-plane that the velocity field is characterized by a relatively high velocity counter-clockwise outer flow starting from the inlet diffuser, moving down through the room, then along the floor, and up towards the room outlet. There are also two smaller, low velocity recirculating zones nested within the main outer flow region.

Figure 5 shows the contours of the temperature in the room at the mid-plane, $y$ = 0. It shows that, despite local differences in the velocity field, this room is close to a well-mixed assumption of uniform temperature. Apart from the colder than average region near the inlet caused by the 14 °C supply air and a very small thermal boundary layer near the heated floor, the majority of this room is

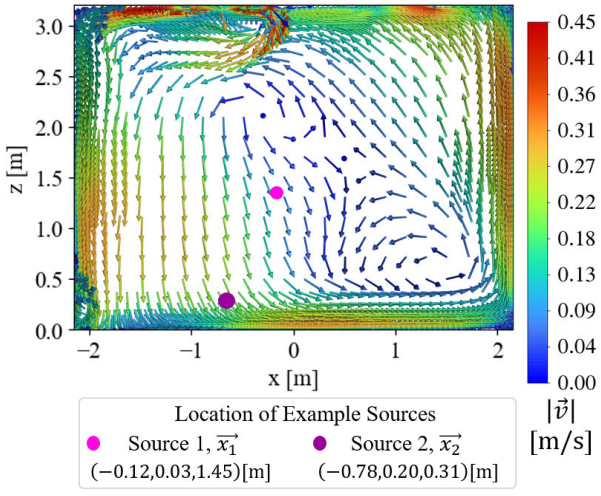


**Fig. 4** Vector field of velocity, $\vec{v}$, at the mid-plane, $y$ = 0, colored by the local velocity magnitude. The locations of the two example sources, discussed in Section 5.2, are also shown projected onto the mid-plane

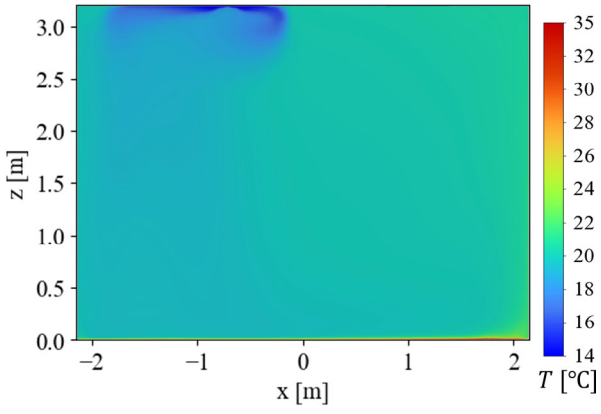


**Fig. 5** Contours of the steady-state temperature field, $T$ [°C], at the mid-plane, $y$ = 0

close to the room set-point temperature of 20 °C, and the entire occupied zone falls within the ASHRAE Standard 55 recommended thermal comfort guidelines (ASHRAE 2020).

## 5.2 General trends of contaminant distribution

In this section, we introduce some of the trends in transient contaminant concentration observed in this room. We first present the transient distribution of concentration from two example sources, discussing the trends during the releasing period and decaying period. We then discuss the impact the releasing duration of a source has on decaying period trends. Finally, we show a contour of the fully-developed relative concentration and discuss the relationship with the steady-state airflow field.

### 5.2.1 *Releasing period*

Figures 6 and 7 show the transient distributions of contaminants in the breathing zone during the releasing and decaying periods, respectively. Two example source locations are used, which are highlighted in Figures 3 and 4. Snapshots of the transient distributions are shown in the form of box and whisker plots at intervals of 1 min. The plots show the median (orange), the interquartile range (*IQR*) (□), and outliers (•) in the set of local concentrations, $\mathcal{C}_{ij}$, for each example source. Here, any points $i$ where $\mathcal{C}_{ij}(t) > 1.5IQR + \text{Q3}$ or $< \text{Q1} - 1.5IQR$, are considered outliers, where Q1 and Q3 are the 1st and 3rd quartiles of the set $\mathcal{C}_{ij}(t)$. These figures also show the source-average concentration, $\overline{\mathcal{C}}_j(t)$, for both sources (blue) and the corresponding well-mixed concentration (grey).

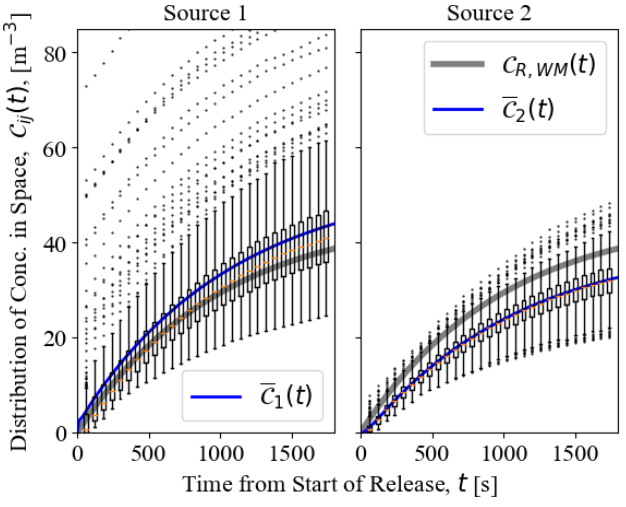


**Fig. 6** Box and whisker plots of the transient distribution of concentration in space during the releasing period, as well as the average concentration, $\overline{\mathcal{C}}_j(t)$ (blue) for two example source locations. Both plots also show the same transient well-mixed concentration, $\mathcal{C}_{R,WM}(t)$ (grey)

Figure 6 shows that during the releasing period in this room, there are noticeable differences in the source average concentration, $\overline{\mathcal{C}}_j$, for the two example source locations. After an 1800 s release, the source average for Source 1 is 13.5% greater than the well-mixed prediction, while for Source 2 it is nearly 16% lower than the well-mixed prediction. There are also major differences in the spatial distribution of concentration from these two sources. For Source 1, there are a significant number of outlying high concentration measuring points, which cause the source-average concentration to be notably higher than the median. In contrast, the contaminants from Source 2 appear to be approximately normally distributed, since the source-average concentration matches closely with the median concentration. There are both high- and low-concentration outliers, indicating that the data set is more clustered near the mean compared to the contaminant distribution from Source 1. Source 1 shows a strong positively skewed distribution with a long tail of high-concentration measuring points which increases the mean, source average, and cause it to be notably higher than the median.

The differences between these two sources can largely be explained by their respective source locations and the local airflow in those areas, shown in Figure 4. For example, Source 1 is located within the rooms occupied breathing-zone, unlike Source 2. The high concentration outliers in the set of local concentrations, $\mathcal{C}_{i1}$, correspond to the measuring points nearby the source location, which see much higher local concentrations. The differences in the source average concentrations reflect how quickly contaminants are removed from a particular regions of the room, and can be used to inform differences in the relative ventilation effectiveness at different source locations. Figure 4 shows that Source 1 is located in a region of relatively low velocity and is also near the two recirculating zones. A large portion of the contaminants released from Source 1 may be trapped in these recirculation zones, increasing the residence time of these airborne contaminants in the room. By comparison, Source 2 is located in a region of relatively high velocity within the main outer flow region. A large portion of the contaminants released from Source 2 are carried by the main outer flow along the floor and up towards the room outlet. The differences in the contaminant dispersion paths away from the particular source locations help to explain the major differences in the transient distributions of contaminants from these two sources.

### 5.2.2 *Decaying period*

Similarly to Figure 6, Figure 7 shows the distribution of local concentrations in the occupied breathing zone for the

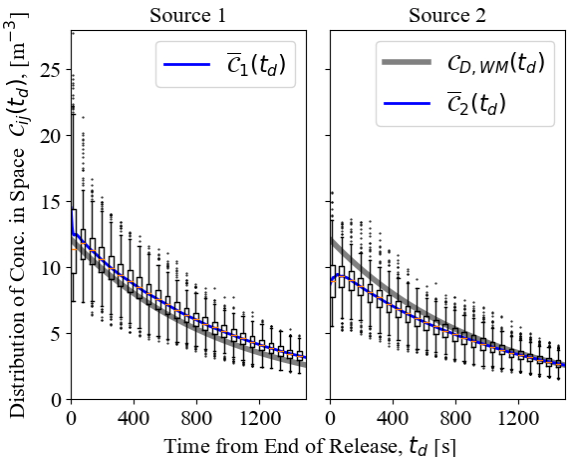


**Fig. 7** Box and whisker plots of the transient distribution of concentration in space during the decaying period, as well as the average concentration, $\bar{C}_j(t_d)$, (blue) for two example source locations, $\vec{x}_j$, noted in Figure 3. Both plots also show the same transient well-mixed concentration, $C_{D,WM}(t_d)$ (grey)

same two example source locations, but for the decaying period after a release of duration $t_{rel}$ = 300 s. Again, we see that the well-mixed assumption underestimates the observed source average concentration for Source 1 while overestimating for Source 2. This difference stems from the differences in the ventilation effectiveness at the two source locations during the releasing period, and the resulting differences in their initial decaying period values, $C_{0,CFD}$. The differences in the general trend of the source average curves during the initial mixing stage are also notable. As we see in Figure 9 for Source 1, the average concentration quickly drops from a high initial concentration before smoothly decaying in a predictable way. By contrast, the average concentration for Source 2 initially increases from some low concentration before reaching a peak, and then decaying in the expected manner. This delayed peak for Source 2 is a result of the time it takes for the majority of the contaminants to move from the source location up and into the breathing zone and thus contribute to the source average measurement.

Similarly, the sharp drop in Source 1's average concentration during the mixing stage can be explained by the rapid dispersion of contaminants away from the region near the source. The high-concentration outlying measuring points near the source quickly move toward the average after the release ends and the contaminants quickly spread throughout the room. This also causes the set of local contaminant concentrations, $C_{i1}$, to quickly become more normally distributed, and the strong positive skew noted in the releasing period quickly dissipates. The distribution of local concentrations, $C_{ij}$, from any source quickly becomes approximately normal in the decaying period. The relative variability of concentration in space for different source locations all approach the same fully-developed relative spatial variability, $\delta^*_{C_i,FD}$, discussed further in Section 5.4.1.

### 5.2.3 *Example of regression curve fitting*

Here we apply the curve fit models to characterize the transient behavior of source average concentration observed in our CFD simulations. Using a least squares regression, the transient behavior of each source is summarized using scalar *fit*-parameters to describe the development of the source average concentrations in time. As we noted in Section 3.3, at the start of both the releasing and decaying periods there is a brief *mixing stage*. During this stage, the slopes of the different source average curves, $\bar{C}_j(t)$, can vary dramatically depending upon the source location and the initial path the contaminants take away from the source as they disperse. Capturing the diverse range of behavior during this brief mixing stage using a curve fit method is impractical. However, after this brief mixing stage all the different source average curves follow smooth paths similar to those predicted by the well-mixed model, Eqs. (2) and (3). We use the term *mixing time*, $t_{mix}$, to describe the duration of this stage at the start of each period before the source average curves take on their smooth predictable forms. While the mixing times can also vary with different source locations, in both periods after approximately 120 s the all the curves have taken on the smooth shapes of Eqs. (12) and (13). Since the concentration time series do not follow these curves during the initial mixing stage, to avoid the confounding influence of this period, we ignore the first 120 s of each period when calculating the fit parameters.

*Releasing period*

Figure 8 shows an example of the releasing period regression curve fit, Eq. (12), being applied to represent the source average concentration from Source 1. A key difference Eq. (12) and the well-mixed average concentration model, Eq. (2), is the addition of the intercept term, $C_{I,R,fit}$. We introduce this term in order to account for the initial shift in the source average concentration which occurs during the mixing stage. Figure 8 also demonstrates why the $C_{I,R,fit}$ term was added to Eq. (12). It compares the result of the three-parameter fit described in Eq. (12) (dashed line) with a similar two parameter fit where we do not attempt to account for this initial shift that occurs during the mixing stage, $C_{I,R,fit}$ = 0 (dotted line). It is clear, particularly in the subfigure, that the three-parameter fit does a much better job of predicting the transient source average than the two-parameter fit. Adding an intercept term is particularly helpful in accurately assessing the observed breathing-zone contaminant removal rates, $1/\tau_{R,fit}$. The variability in set of calculated intercept terms also enables us to better understand

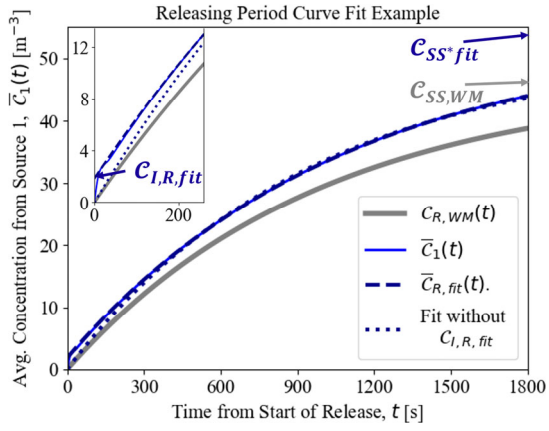


**Fig. 8** Breathing-zone average concentration from Source 1 (blue), the releasing-period curve-fit (navy) for this source of the form shown in Eq. (12), and the concentration predicted by the well mixed model (grey)

how uncertainty in a particular input parameter can influence the magnitude of uncertainty in this mixing stage behavior.

*Decaying period*

Figure 9 shows an example of the decaying period curve fit, Eq. (13), for Source 1 after a $t_{rel}$ = 300 s release. In this figure, we see that shortly after a brief mixing stage the source average concentration is very well described by the Eq. (13). We also point out that the mixing stage shift in concentration, $C_{I,D,fit}$ = 1.79 [m$^{-3}$], is similar to the initial shift in concentration during the releasing stage, $C_{I,R,fit}$ = 1.84 [m$^{-3}$], and we find that this is the case for all the different source locations tested, with $C_{I,D,fit} \approx C_{I,R,fit}$ for any particular source location.

We computed similar fits for each source average concentration, giving us a varying set of 50 instances for each parameter. The variability in these sets of fitting parameters

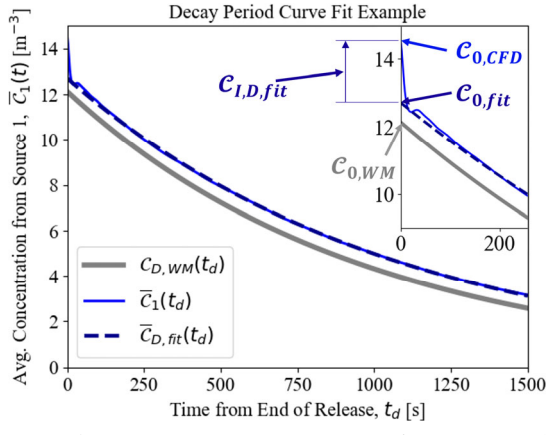


**Fig. 9** Breathing-zone average concentration from Source 1 (blue), the decay-period curve-fit (navy) for this source of the form shown in Eq. (13), and the concentration predicted by the well mixed model (grey)

can then be analyzed to understand how the average concentration varies in response to our uncertain input parameter, i.e. does variability in the source location influence the room time constant, the average magnitude, or the mixing stage behavior? Some of the *fit*-parameters may be more sensitive to changes in source location while others are not, but maybe affected by other uncertain room parameters. This enables us to better understand how to incorporate the impact of different uncertain input parameter on the spatiotemporal variability in the average concentration.

### 5.2.4 *Impact of releasing time on the decaying period concentration*

In previous sections, we showed examples of the decaying period after a $t_{rel}$ = 300 s release. In this section, we discuss the trends in the decaying period as $t_{rel}$ increases from 15 s to a continuous release, $t_{rel} = \infty$, for a single example source. Figure 10(a) shows the trends in the average concentration from Source 1, $\bar{C}_1$. Because all of these releases of different duration's are generated by superimposing the same instantaneous release, the different $\bar{C}_1$ curves overlap while $t < t_{rel}$. For each finite release, the source averages appear to follow a similar pattern during the decaying period also. We can see in Figure 10(a) that the sharp drop in the source average during the decaying period mixing stage, $C_{I,D,fit}$, is of a similar magnitude, and appears to take a similar amount of time, $t_{mix}$, regardless of the releasing duration. Both these observations support the explanation that this abrupt shift during the mixing stage is a result of the high concentration region near Source 1 quickly dissipating just after the release. Due to the nature of the contaminant release and steady airflow, the same absolute amount of recently released contaminants will be in these high-concentration regions and take the same amount of time to move out of it. For this source location, there is a sharp dip in the source average during the mixing stage. Figure 13 shows that this constant magnitude shift has a greater impact on the the mixing stage model accuracy when the release is shorter and the recently released contaminants make up a larger fraction of all the contaminants in the room. We see for $t_{rel}$ = 15 s the $\bar{C}_1$ curve dips below the fitted curve during this stage approximately by approximately 30% of $C_{0,WM}$ but for longer releases, such as $t_{rel}$ = 300 s shown in Figure 9, the magnitude of this dip is negligible.

Figure 10(b) shows the same set of source average concentrations, but only during the decaying period and also normalized by their respective well-mixed initial decaying period concentrations, $C_{0,WM} = C_{R,WM}(t_{rel})$. A brief examination of Eqs. (2) and (3) shows that $C_{0,WM}$ is proportional to the total amount of contaminants released

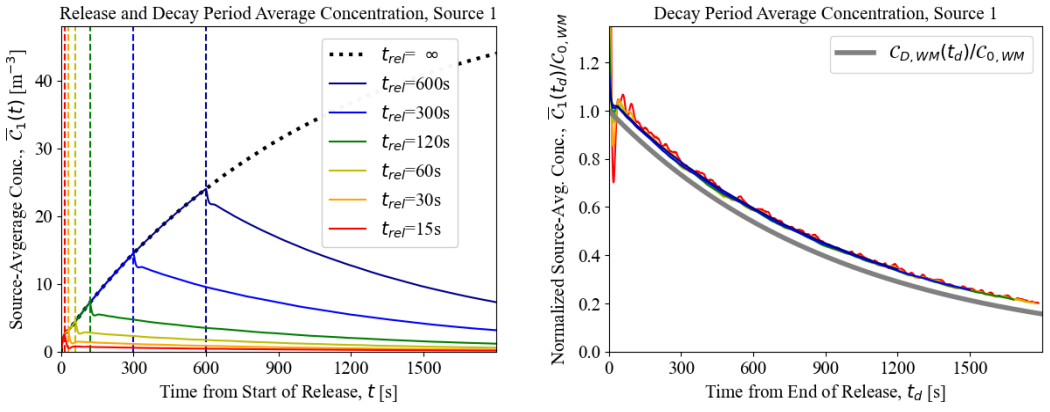


(a) Releasing and decaying periods (b) Normalized decaying period

**Fig. 10** Source-average concentration from Source 1, $\bar{C}_1$, shown for increasing releasing times, $t_{rel}$. (a) shows both the releasing and decaying periods for finite releases ranging from 15 s < $t_{rel}$ < 600 s (solid colored), as well as a continuous releasing case (dotted black). (b) shows the same data, during only the decay-period, and normalized by the predicted well-mixed initial decay-period concentration, $C_{0,WM}$ (solid colored), as well as the well-mixed decay-period concentration, $C_{D,WM}(t_d)$, equivalently normalized (grey)

over a period $t < t_{rel}$. We note that the different source average curves decay at the same rate regardless of the total amount of contaminant or length of release. In the terms of the curve fit model, Eq. (3), for a given source location the terms $C_{0,fit}/C_{0,WM}$ and $\tau_{D,fit}$ are extremely consistent for different release durations. Because of these observed consistencies in the decaying period behavior and for the sake of brevity, the rest of this work will focus on the trends in the decaying period after a $t_{rel}$ = 300 s release.

### 5.2.5 *Fully-developed relative concentration*

In this section, we discuss the link between the spatial variability in the velocity field and the distribution of the contaminant concentration in space. Figure 11 shows the contours of the relative concentration distribution from Source 1 at the mid-plane, $y$ = 0, well into the decaying period, $t_d$ = 900 s. This plot was generated using a quadratic interpolation of the measured concentrations from the sets of the equally spaced full-room (×) and breathing zone (+) sets of measuring points, $\vec{x}_i$, where $y_i$ = 0.

In comparing Figures 4 and 11, we can see that there is a strong correlation between the velocity field and the relative concentration field. The regions of lower than average concentration correspond with regions of higher than average velocity, and regions of higher concentration correspond to areas of lower velocity. The relative spatial distribution of the concentration well into the decaying period, $t_d \gg t_{mix}$, depends almost entirely on the airflow in the room. After examining similar contours to Figure 11 for a subset of the sources at various points in the releasing and decaying periods, we found that during the releasing period and mixing stage the concentration field depends upon the source location. However, well into the decaying period, the relative concentration fields are nearly constant and identical to the cross-section of the fully-developed field shown in Figure 11. We will refer to this common level of relative spatial variability for different source locations long into the decay period that as the *fully developed spatial variability*, $\delta^*_{C_i,FD}$. Once the concentration field reaches this fully developed point, contaminant concentration everywhere in the room decays uniformly at a rate proportional to the local concentration, which causes the relative concentration field to remain constant.

While the fully developed level of relative spatial variability, $\delta^*_{C_i,FD}$, is not influenced by the source location, the average concentration is strongly influenced by the source location within the flow field. We observed that this fully-developed concentration field also predicts how well

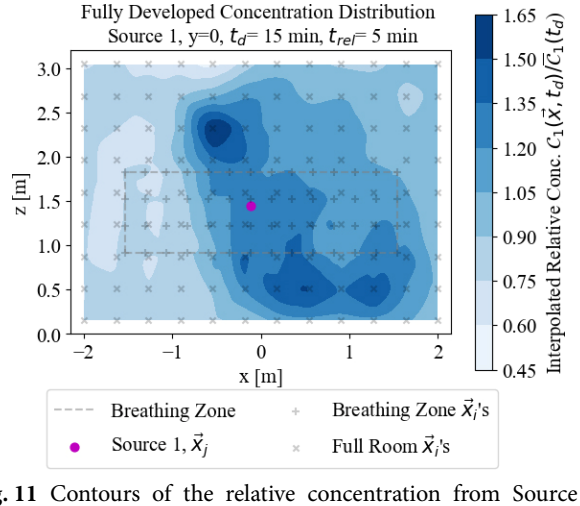


**Fig. 11** Contours of the relative concentration from Source 1, interpolated from the measuring points (grey × and +) at the room mid-plane, $y_i$ = 0. The boundary of the breathing-zone (grey dashed) and the location of Source 1 (pink) are also shown

contaminants are removed from a given location. The regions in the fully-developed field with low relative concentrations, $\mathcal{C}_j(\vec{x},t_d)/\overline{\mathcal{C}}_j < 1$ in Figure 11, tend to be the regions from which the contaminant sources are removed more efficiently, and likewise sources that are removed less efficiently (higher $\mathcal{C}_{ss,fit}$ and $\mathcal{C}_{0,fit}$ terms) are often located in regions where in the fully-developed field $\mathcal{C}_j(\vec{x},t_d)/\overline{\mathcal{C}}_j > 1$. This indicates that when designing a space the fully-developed relative concentration field can provide significant insight into the levels of spatial variability in a room and how best to reduce this spatial variability by eliminating these high concentration zones.

## 5.3 Variability in room average measures

In this section, we discuss the variability in the source-average transient behavior of the room due to different source locations. We first present the source-average concentration from all 50 of the CFD-simulated sources for both the releasing and decaying periods. We also discuss the insights which can be gained about the trends in these average concentrations using our proposed curve fitting regression model, and discuss the relationship between the source location and the trends in the source average concentration. And finally, we present the observed variability in the source-average exposures in both periods.

### 5.3.1 *Variability in average concentration*

*Releasing period*

Figure 12 shows the set of all 50 source-average concentrations, $\overline{\mathcal{C}}_j(t)$, during the releasing period as well as the total-average concentration, $\overline{\mathcal{C}}_{ij}(t)$. There is significant variability in the observed source averages, and they often deviate significantly from the well-mixed prediction. At $t$ = 1800 s, the observed source average concentrations in this study ranged from 82%–130% of the well-mixed prediction, with the total average equal to approximately 114% of the well-mixed concentration. In summation, during the releasing period the well-mixed assumption tends to under predict the contaminant concentration in this room's breathing zone.

The releasing period *fit*-parameters ($\mathcal{C}_{I,fit}$, $\mathcal{C}_{SS,fit}$, and $\tau_{R,fit}$) are described in Eq. (12) in Section 3.3 and are summarized Table 1. There are several trends in the variability of the source average during the releasing period that can be better understood using the distributions of these *fit*-parameters. First, the term representing the constant shift in the concentration resulting from to the initial mixing stage, $\mathcal{C}_{I,R,fit}$, is small relative to the main scaling term, $\mathcal{C}_{SS,fit}$. The different $\mathcal{C}_{I,R,fit}$'s range from −3.8% to 7.0% of the $\mathcal{C}_{SS,WM}$ term, with a mean of $\overline{\mathcal{C}_{I,R,fit}}$ = 0.3% of $\mathcal{C}_{SS,WM}$, close to the well

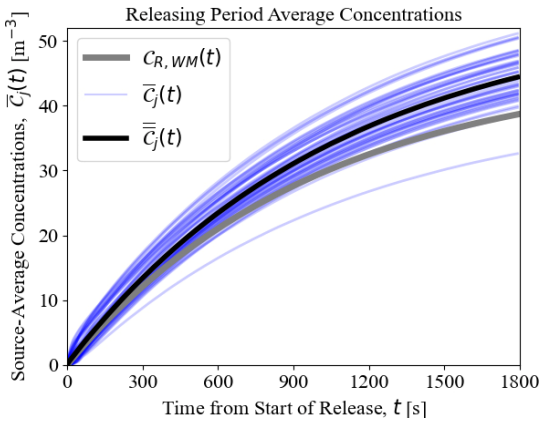


**Fig. 12** Releasing period breathing-zone source-averaged concentrations from each of the 50 source locations (blue), as well as the total average (black) and the expected well-mixed (grey) concentrations

mixed intercept of 0. The relatively small average magnitude of this initial offset, $\left|\overline{\mathcal{C}_{I,R,fit}}\right|$ = 3% of $\mathcal{C}_{SS,WM}$, means that for long releases when the concentration in the room is at or near a steady-state level the significance of this initial offset is minimal, but in situations when the releasing duration is short and the and the peak concentration is significantly less than $\mathcal{C}_{SS,WM}$, this initial deviation can cause differences between the well-mixed model and spatially resolved predictions of a room's average concentration.

On average the scaling term, $\overline{\mathcal{C}}_{SS,fit}$, is 18% higher than its well-mixed equivalent, $\mathcal{C}_{SS,WM}$, and ranges from 9% lower to 31% higher than the well-mixed value. The absolute variability in the set of $\mathcal{C}_{SS,fit}$ terms was notably higher than for $\mathcal{C}_{I,R,fit}$, with $s_{\mathcal{C}_{SS,fit}}$ = 7.1% of $\mathcal{C}_{SS,WM}$. This indicates that for longer releases the initial variability related to the mixing stage offset has less of an impact on the overall variability in the average than the variability in the $\mathcal{C}_{SS,fit}$ term. The set of observed average time constants $\tau_{R,fit}$ is notably less variable than either $\mathcal{C}_{SS,fit}$ or $\mathcal{C}_{I,R,fit}$, with a relative variability of $\delta^*_{\tau_{R,fit}}$ = 1.5%. This indicates that while the overall magnitude of the concentration can vary significantly with different source locations, the average rate of contaminate removal, $1/\tau_{R,fit}$, is not significantly impacted by where in the room a source is located. It is also important to note that the observed contaminant removal rate in this room is consistently lower than that of the well-mixed model, with $\overline{\tau}_{R,fit}$ 11% higher than $\tau_{WM}$.

By understanding the relative levels of variability in the underlying parameters describing the transient behavior, as well as the way these parameters relate to the average, we can better explain the trends we see in the relative variability in $\overline{\mathcal{C}}_j(t)$, shown in Figure 13. The relative variability is very high during the mixing stage because the average concentration in the room is very low and there is significant variability in the mixing stage behavior, represented by $\delta_{\mathcal{C}_{I,R,fit}}$

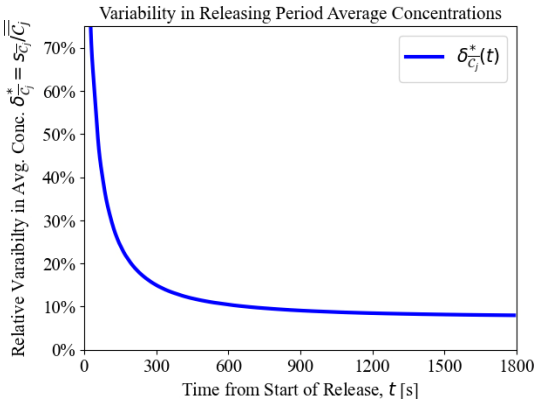


**Fig. 13** Relative variability in the set of transient source-average concentrations during the releasing period

which is large relative to $\bar{C}_j$ at this time. The relative variability in the observed averages quickly decreases after the mixing stage however, and appears to approach a constant steady-state value near 7%. Because of the minimal variability in the time constant terms, $\tau_{R,fit}$, this variability in set of averages long after the mixing period is equivalent to the relative variability in the set of steady-state concentration terms, $\mathcal{C}_{SS,fit^*}$.

*Decaying period*

Figure 14 shows the set of all 50 decaying period source-average concentrations, $\bar{C}_j(t_d)$, and the total-average concentration, $\bar{\bar{C}}_{ij}(t_d)$. Similarly to the releasing period, on average in this room the concentration during the decaying period is consistently higher than what the well-mixed model would predict. During the initial mixing stage when the source average is highest, there is significant variability in both the initial decaying period concentration, $\mathcal{C}_{0,CFD}$, and in the initial path that the source average curve takes. The $\mathcal{C}_{0,CFD}$ terms range between 71% and 142% of the well-mixed initial decaying period concentration, $\mathcal{C}_{0,WM}$, with

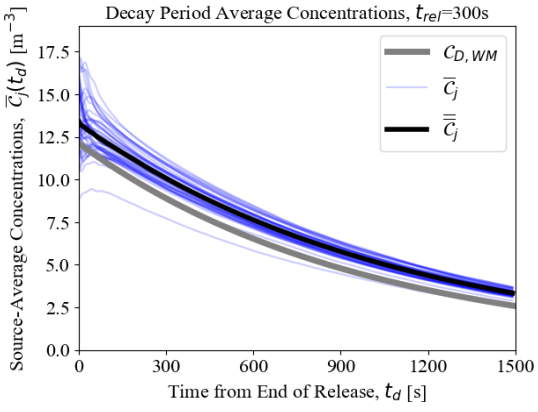


**Fig. 14** Decaying period breathing-zone source-averaged concentrations from each of the 50 source locations (blue), as well as the total average (black) and the expected well-mixed (grey) concentrations

$\bar{\mathcal{C}}_{0,CFD}$ =109% of $\mathcal{C}_{0,WM}$ and a relative standard deviation of $\delta^*_{C_0,CFD}$ = 15%. This initial variability is by definition equivalent to the variability in the source averages during the releasing period at $t_{rel}$ ($t$ = 300 s in Figure 12). Figure 14 also shows how the shapes of the source average curves from different source locations during the mixing stage. As shown in the example sources, the behavior in this period is strongly tied to the source location within the local airflow and the trajectories that contaminants follow just after they are released from a particular source location.

There are several notable observations from the distribution of decaying period *fit*-parameters, which are all summarized in Table 1. The calculated $\mathcal{C}_{0,fit}$ terms range from 82% to 123% of $\mathcal{C}_{0,WM}$, with $\bar{\mathcal{C}}_{0,fit}$ = 108% and $s_{\mathcal{C}_{0,fit}}$ = 7.4% of $\mathcal{C}_{0,WM}$. Indicating that $\mathcal{C}_{0,fit}$ is significantly impacted by the source location. While the set of observed decaying period time constants, $\bar{\tau}_{D,fit}$, was nearly identical to the set $\bar{\tau}_{R,fit}$ and was not impacted by the source location. The higher initial average concentration and average time constant, relative to those of the well-mixed model, results in a higher average concentration than the well-mixed prediction throughout this period. This consistently higher concentration would lead to significantly higher levels of exposure during this period compared to the well-mixed model's prediction.

Figure 15 shows the transient development of the relative variability in the decaying period source averages, $\delta^*_{\bar{C}_j}(t_d)$. Similar to the releasing stage, the variability is significantly higher during the mixing stage, then approaches a constant, lower level of variability. This constant level is approximately equivalent to the variability observed in the set of scaling terms, $\mathcal{C}_{0,fit}$.

### 5.3.2 *Variability in curve fit parameters*

Several of the parameters in Eqs. (12) and (13) have the same or analogous meanings, and are therefore similarly effected by variability in particular room parameters. Table 1

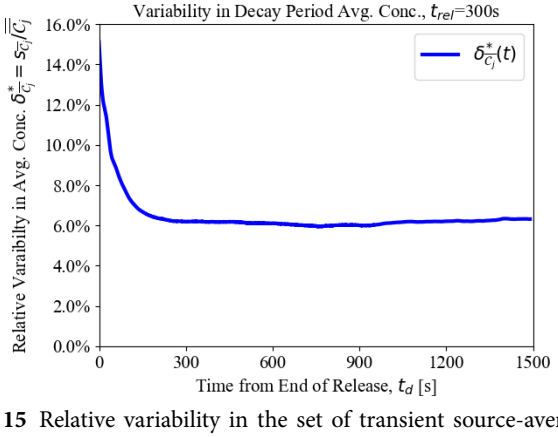


**Fig. 15** Relative variability in the set of transient source-average concentrations during the decaying period

**Table 1** Summary of the distribution of each curve-fit parameter for the set of 50 different source locations. It includes the minimum, mean, and maximum value of each of the corresponding parameter sets, as well as their standard deviations and the mean-normalized standard deviations of each set

| | Parameter, $X$ | Units | Well-mixed value | Min. $X$ | $\overline{X}$ | Max. $X$ | $s_X$ | $\delta^*_X$ |
|---|---|---|---|---|---|---|---|---|
| Releasing | $\tau_{R,fit}$ | [s] | 969 | 1032 | 1080 | 1114 | 16.7 | 1.5% |
| | $\mathcal{C}_{SS,fit}$ | [m$^{-3}$] | 46.2 | 42.1 | 54.7 | 60.2 | 3.3 | 6.0% |
| | $\mathcal{C}_{SS,fit^*}$ | [m$^{-3}$] | 46.2 | 40.9 | 54.8 | 62.3 | 4.0 | 7.2% |
| | $\mathcal{C}_{I,R,fit}$ | [m$^{-3}$] | 0 | −1.8 | 0.2 | 3.2 | 1.6 | — |
| | $\lvert\mathcal{C}_{I,R,fit}\rvert$ | [m$^{-3}$] | 0 | 0.1 | 1.4 | 3.2 | 0.78 | 57.1% |
| Decaying | $\tau_{D,fit}$ | [s] | 969 | 1032 | 1080 | 1114 | 17.0 | 1.6% |
| | $\mathcal{C}_{0,fit}$ | [m$^{-3}$] | 12.3 | 10.1 | 13.3 | 15.2 | 0.9 | 6.8% |
| | $\mathcal{C}_{0,CFD}$ | [m$^{-3}$] | 12.3 | 8.8 | 13.4 | 17.4 | 2.0 | 15.2% |
| | $\mathcal{C}_{I,D,fit}$ | [m$^{-3}$] | 0 | −1.8 | 0.1 | 3.3 | 1.6 | — |
| | $\lvert\mathcal{C}_{I,D,fit}\rvert$ | [m$^{-3}$] | 0 | 0.1 | 1.4 | 3.3 | 0.78 | 55.9% |

demonstrates the similarities between the calculated distributions of particular releasing and decaying period *fit*-parameters. First, the room time constants calculated during the two periods, $\tau_{R,fit}$ and $\tau_{D,fit}$ are nearly identical for any particular source location. The observed room time constants were significantly higher than the well-mixed model would predict and did not appear to be too dependant on the source location. The distributions of the terms describing the mixing stage offsets in the two periods are also nearly identical for any given source location, $\mathcal{C}_{I,D,fit} \approx \mathcal{C}_{I,R,fit}$. Figure 10(a) shows the magnitude of $\mathcal{C}_{I,D,fit}$ was also consistent regardless of $t_{rel}$. Together this indicates that the shift which occurs during the mixing stage is extremely consistent for a given releasing location regardless of the releasing duration since it is a result of the initial path the contaminants take just after they are released.

Unlike the room time constant terms however, the sets of intercept terms, $\mathcal{C}_{I,R,fit}$ and $\mathcal{C}_{I,D,fit}$, are highly variable and extremely sensitive to the source location. Both sets of $\mathcal{C}_{I,fit}$ terms have bi-modal distributions with their means centered near 0, but with an average magnitude of $\left|\overline{\mathcal{C}_{I,fit}}\right| = 1.4$ [m$^{-3}$], or 2.6% of the predicted steady-state concentration, $\overline{\mathcal{C}}_{SS,fit^*}$, and could be as high as 6% of $\overline{\mathcal{C}}_{SS,fit^*}$. The uncertainty in this mixing stage offset term due to the source location is less critical in situations with long releasing periods when variability in the $\mathcal{C}_{SS,fit}$ term dominates, but for shorter duration releases when $\mathcal{C}_{0,fit}$ is closer to $|\mathcal{C}_{I,D,fit}|$, this initial decaying period variability is much more significant. The variability in the decaying period exposure, and specifically $\delta^*_{C_0,fit}$, will be much higher for short release cases due to the relative contribution of the consistent-magnitude mixing stage shift. Finally, the main linear scaling terms, $\mathcal{C}_{SS,fit}$ and $\mathcal{C}_{0,fit}$, also have similar distributions and are highly correlated for the same source locations, with higher values of $\mathcal{C}_{SS,fit}$ corresponding to higher values of $\mathcal{C}_{0,fit}$ for the same source location. High values of $\mathcal{C}_{SS,fit}$ also correlate with higher positive values of $\mathcal{C}_{I,fit}$. Each of these terms are strongly influenced by the source location and inform how effectively contaminants are removed from different parts of the room.

### 5.3.3 *Variability in average exposure*

*Releasing period*

Figure 16 shows the source-average exposures for each source location tested, as well as the mean-averaged exposure and the expected exposure in a well-mixed room for the releasing period. During the releasing period, the transient exposure continues to increase even after the concentration approaches its steady-state value. As a result, for long releases, the exposure accumulated during the initial mixing stage is less significant to the overall exposure, which depends primarily on the steady-state average and spatial distribution of concentration. However, for shorter releases, the high mixing stage variability has a more significant impact

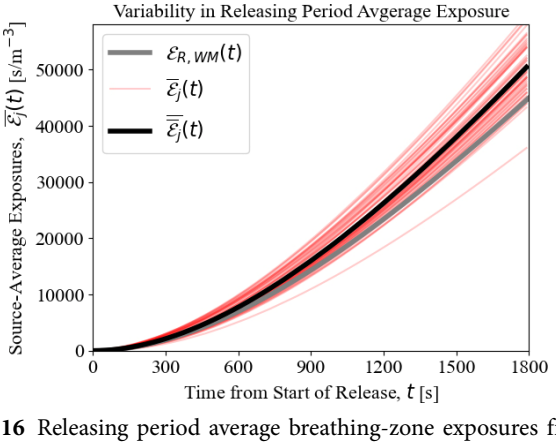


**Fig. 16** Releasing period average breathing-zone exposures from each of the 50 source locations (red), as well as the total average (black) and the expected well-mixed exposures (grey)

on the overall exposure. Since the concentration observed in CFD for this room is consistently higher than the well-mixed assumption would predict, the CFD-predicted exposures increasingly deviate from the well-mixed exposure as time goes on. After the 1800 s (30 min) continuous release shown in Figure 16, the source average exposure from different source locations can range from $\overline{\mathcal{E}}_j$ = 80% to 133% of the well-mixed exposure, $\mathcal{E}_{WM}$, with a total average exposure of $\overline{\overline{\mathcal{E}}}_j$ = 112% and a standard deviation of $s_{\overline{\mathcal{E}}_j}$ = 11% of $\mathcal{E}_{WM}$.

*Decaying period*

Figure 17 shows the source-averaged exposures, $\overline{\mathcal{E}}_j$, for each source location tested, as well as the total-average exposure and the expected exposure in a well-mixed room for the decaying period. In contrast to the releasing period, the highest rate of exposure accumulation occurs during the initial mixing stage of the decaying period, shown by the slope of the source average curves which is greatest early in the decaying period. As this period progresses, the average concentration in the room decreases and the different source average exposure curves approach some final steady-state value when the all of the contaminants have been removed from a given room. Again, because the average concentrations are higher and decay slower compared to the well-mixed model, the well-mixed model tends to underestimate the level of exposure in this room and the deviation gets worse as time increase, until reaching some final value when all the contaminants are removed in both models. At the end of decaying period shown in Figure 17 ($t_d$ = 1500 s), the observed source average exposures deviate significantly from the well-mixed prediction; ranging from $\overline{\mathcal{E}}_j$ =120% to 177% of the well-mixed exposure, $\mathcal{E}_{WM}$, with a total average exposure of 158% of $\mathcal{E}_{WM}$ and a standard-deviation 10% of $\mathcal{E}_{WM}$.

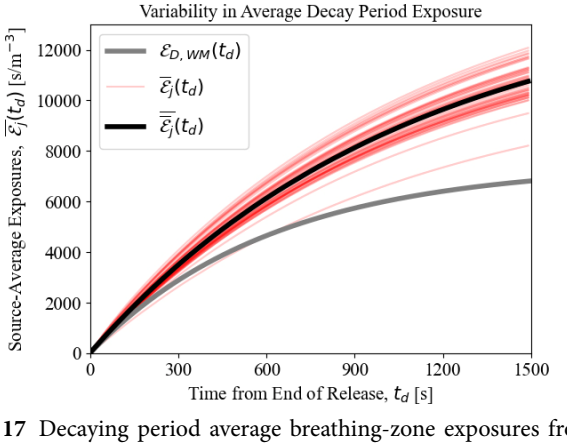


**Fig. 17** Decaying period average breathing-zone exposures from each of the 50 source locations (red), as well as the average of these transient averages (black) and the expected well-mixed exposure (grey)

## 5.4 Measures of variability in space

This section discusses how the concentration and resulting exposure can vary in space within a particular room, relative to the corresponding source-average. First we discuss the variability of concentration in space for both the releasing and decaying period, and then similarly discuss the variability of exposure in space.

### 5.4.1 *Variability of concentration in space*

*Releasing period*

Figure 18 shows the set of relative spatial variabilities for the 50 source locations, $\delta^*_{\overline{C}_j}$, during the releasing period. Initially, the relative variability approaches infinity since the denominator, $\overline{C}_j$, is zero at $t$ = 0, and the contaminants are concentrated near the releasing location. As time goes on, each source asymptotically approaches a source-specific level of relative steady-state spatial variability, $\delta^*_{C_{ij},SS}$. Many of the sources have reached this $\delta^*_{C_{ij},SS}$ value by the end of the $t$ = 1800 s continuous release, but some of the sources, particularly those approaching higher $\delta^*_{C_{ij},SS}$ values are still decreasing. At this point, the spatial variability can range between $\delta^*_{C_{ij}}$ = 11% and 40% of the rooms source average concentration, with an average of $\overline{\delta}^*_{C_{ij}}$ = 22% and an associated standard deviation of $s_{\delta^*_{C_{ij}}}$ = 7.2% of the corresponding source average. With an average variability in spaces of 22% and a steady-state variability in the different averages of approximately 7%, we can say that in this room the relative spatial variability was nearly three times greater than the relative variability in the room average concentration for an uncertain source location. This indicates that, for this room on average, an occupant's location within the breathing zone has more influence on the transient levels of concentration they will see than the location of the source within the room.

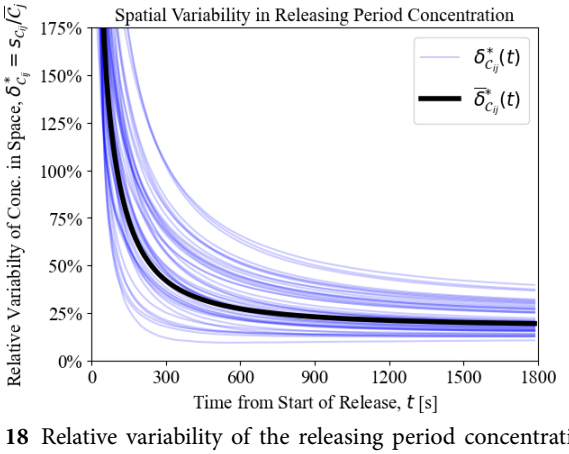


**Fig. 18** Relative variability of the releasing period concentration in space for each of the 50 source locations (blue), as well as the transient average this set of relative-variabilities

As shown previously in Figure 6, for some source locations (especially those within the breathing zone) the measured distribution of concentration in space can be extremely positively skewed with a small number of very high concentration monitoring points near the source. These source locations which produce highly skewed distributions also tend to correspond with higher levels of steady state variability, $\delta^*_{C_{ij},SS}$.

*Decaying period*

Figure 19 shows the set of relative spatial variabilities during the decaying period after a $t_{rel}$ = 300 s release. Similarly to the source average, due to the use of superposition, the initial spatial variability in comes from $t$ = 300 s in Figure 18, and it varies greatly for different source locations. After the initial mixing stage however, the different source scenarios converge to the same fully developed level of spatial variability, $\delta^*_{C_i,FD}$. The subfigure within Figure 19 shows the different paths the $\delta^*_{\bar{C}_j}$ curves take during this mixing period. But by approximately $t_d$ = 300 s, all the sources reach a constant $\delta^*_{C_i,FD}$ = 15%, which is extremely consistent across the different source locations tested. At $t_d$ = 300, the spatial variabilites range from only $\delta^*_{\bar{C}_j}$ = 13% to 16% with a standard deviation of only $s_{\delta^*_{\bar{C}_{ij}}}$ = 0.5%.

It is also notable that for some source locations the steady-state spatial variability, $\delta^*_{C_{ij},SS}$ shown in Figure 18, ends up being lower than $\delta^*_{C_i,FD}$. These sources are likely located in regions that have lower than average concentration in the fully-developed field, i.e. regions in Figure 11 where the relative concentration is less than one. If the source is in this region, the associated higher concentration near the source during the release can cause the overall spatial distribution of concentration to become slightly more uniform. These areas of low concentration also tend to correspond to higher local flow velocities, which also help to explain why the sources with the lowest values of $\delta^*_{C_{ij},SS}$ tend to reach these levels most rapidly, because the contaminants spread out from these locations most quickly.

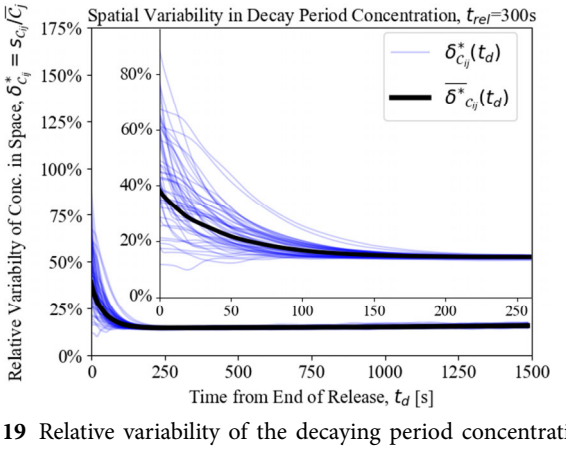


**Fig. 19** Relative variability of the decaying period concentration in space for each of the 50 source locations (blue), as well as the transient average of this set of relative-variabilities (black). The figure also shows a zoomed-in subfigure of the period $t_d$ < 260 s to highlight the variability in the initial mixing stage

### 5.4.2 *Variability of exposure in space*

*Releasing period*

Similarly to the concentration, the releasing period relative-variability of exposure in space, $\delta^*_{\mathcal{E}_{ij}}$ shown in Figure 20, begins as nearly infinity before decreasing towards different steady-state levels that depend upon the specific source location, referred to as $\delta^*_{\mathcal{E}_{ij},SS}$. Because exposure accumulates at specific points in space, the relative spatial variability in exposure tends to be slightly higher than the corresponding relative spatial variability in concentration. This is due to points that, over time, tend to see significantly higher or lower concentration than the room average, which causes the variability to increase as the extremes continue to diverge, relative to the mean. At the end of the $t$ = 1800 s continuous release, the standard deviation in the set of locally measured exposures range from $\delta^*_{\mathcal{E}_{ij}}$ = 9.5% to 56% of the room's average exposure, with an average of $\overline{\delta}^*_{\mathcal{E}_{ij}}$ = 28%, and $s_{\delta^*_{\mathcal{E}_{ij}}}$ =11%.

*Decaying period*

Unlike the spatial variability in the decaying period concentration, the initial spatial variability in the decaying period exposure does not come directly from the releasing period ($t$ = $t_{rel}$ in Figure 20), rather these initial values reflect the variability in space of the instantaneous exposures in each room at $t_{rel}$, i.e., the distribution of local concentrations multiplied by the time integration time-step, $\mathcal{C}_{ij}\Delta t$. Because $t_{rel}$, $t_d$ = 0, is also the point of the highest variability in $\mathcal{C}_{ij}$, the different relative spatial variabilities in exposure, $\delta^*_{\mathcal{E}_{ij}}$, decay towards some fully developed state, but unlike for concentration this fully developed level does

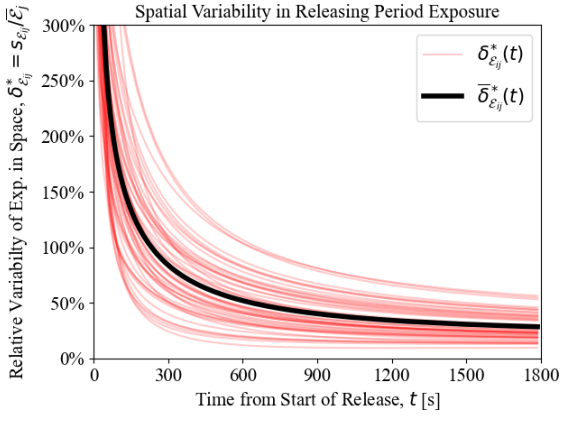


**Fig. 20** Relative variability of exposure in space for each of the 50 source locations during the releasing period (red), as well as the transient average this set of relative-variabilities (black)

vary somewhat with different source locations. The impact of the exposure accumulated during the mixing stage when concentration is highest causes the $\delta^*_{\mathcal{E}_{ij}}$ curves to decay towards a fully-developed state more slowly than the spatial variability in concentration. The difference in these decay rates can be seen by comparing the subfigure windows in Figures 21 and 19. At the end of the $t_d$ = 1500 s decaying period shown in Figure 21, the most of the sources have reached this fully-developed spatial variability. The average spatial variability in exposure is close to $\delta^*_{\mathcal{C}_i,\mathrm{FD}}$, $\overline{\delta}^*_{\mathcal{E}_i,\mathrm{FD}}$ = 15%. However although for most of the decaying period each source location has the same fully developed level of spatial variability in the concentration field, $\delta^*_{\mathcal{C}_i,\mathrm{FD}}$, the differences in the exposure accumulated during the high-concentration, highly-varying mixing stage lead to the observed differences in the fully developed spatial variability in exposure. The relative spatial variability can range from 11% to 19% with $s_{\delta^*_{\mathcal{E}_{ij}}}$ = 1.8% compared to 0.5% for $\delta^*_{\mathcal{C}_i,\mathrm{FD}}$.

## 5.5 Total spatiotemporal variability

In this section, we bring together the trends in the average variability with the trends in spatial variability to examine the total variability in the of observed concentration and exposures in this space from all possible source locations, $\mathcal{C}_{ij}$ and $\mathcal{E}_{ij}$. Figures 22 and 23, concentration and exposure respectively, also demonstrate both the releasing and decaying period trends by depicting the case of a finite release of $t_{rel}$ = 300 s followed by a 1500 s decaying period.

### 5.5.1 *Total variability in concentration*

Figure 22 summarizes the total range of possible breathing zone concentrations in this room for this finite release case with an unknown source location. The darker-shaded region shows the inner 95th quantile for the set of source average concentrations, $\overline{\mathcal{C}}_j$, while the lighter-shaded region shows the same quantile for the full set of local concentrations, $\mathcal{C}_{ij}$. As shown in Section 5.3.1, for both periods the distribution of $\overline{\mathcal{C}}_j$ becomes approximately normal after the mixing stage, and the total average during both periods is consistently higher than well-mixed prediction. During the releasing period, $t < t_{rel}$, there is significant positive skew in the set of local concentrations, resulting from the regions of high concentration near the particular source locations, and the absolute level of spatial variability reaches its peak at the $t_{rel}$. Considering the set of relative spatial variabilities at this point ($t$ = 300 s in Figure 18) we can see that for most of the source locations tested, the room is far from its steady-state level, $\delta^*_{\mathcal{C}_{ij},\mathrm{SS}}$. During the decaying period mixing stage, this skewness is quickly reduced until after the total distribution of $\mathcal{C}_{ij}$ also becomes approximately normal and, as shown in Figure 19, the relative level of spatial variability for each source location reaches the fully developed level, $\delta^*_{\mathcal{C}_i,\mathrm{FD}}$. After this point the levels of relative variability in both the room average and in space reach a constant levels and as a result the total variability in concentration decreases proportionately to the decay in the total average, as shown in Figure 22.

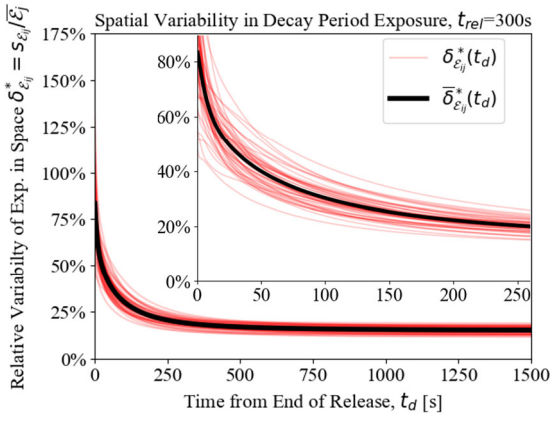


**Fig. 21** Relative variability of exposure in space for each of the 50 source locations during the decaying period (red), as well as the transient average this set of relative-variabilities (black). The figure also shows a zoomed-in subfigure of the period $t_d$ < 260 s to highlight the variability in the initial mixing stage

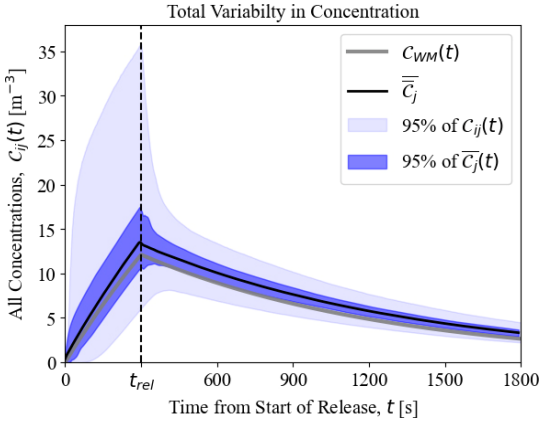


**Fig. 22** The total variability in the set of observed concentrations, $\mathcal{C}_{ij}$, summarized with the inner 95th quantile of the entire set $\mathcal{C}_{ij}$ (light-red), and of the set of source-average concentrations $\overline{\mathcal{C}}_j$ (darker-red), as well as the total-average $\overline{\mathcal{C}}_{ij}$ (black), and well-mixed (grey) concentrations, for a $t_{rel}$ = 300 s release and 1500 s decaying period

### 5.5.2 *Total variability in exposure*

Figure 23 summarizes the variability in the total set of observed local exposures, $\mathcal{E}_{ij}$, for the same finite releasing period shown in Section 5.5.1. The darker-shaded region shows the inner 95th quantile for the set of source-average exposures, $\overline{\mathcal{E}}_j$, while the lighter-shaded region shows the same quantile for the set $\mathcal{E}_{ij}$. As shown in Section 5.3.3, because the source average concentrations are consistently

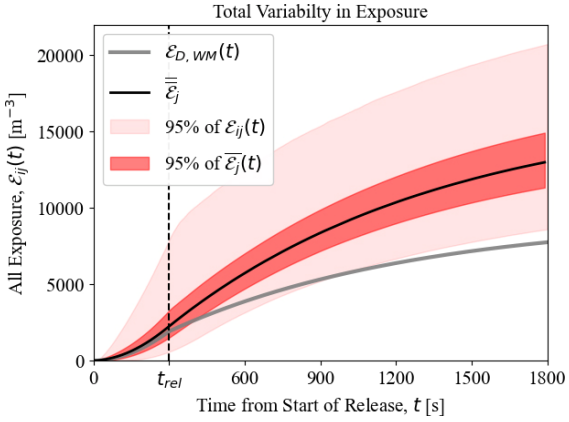


**Fig. 23** The total variability in the set of observed exposures, $\mathcal{E}_{ij}$, summarized with the inner 95th quantile of the entire set (light-red), and of the set of source-averaged exposures $\overline{\mathcal{E}_j}$ (darker-red), as well as the total-average $\overline{\mathcal{E}_{ij}}$ (black dashed), the mean-averaged $\overline{\overline{\mathcal{E}_j}}$ (black solid), and well-mixed (grey) exposures, for a $t_{rel}$ = 300 s release and 1500 s decaying period

higher than the well-mixed concentration the total average exposure predicted by CFD diverges more and more rapidly from the well-mixed prediction with increasing time. The low observed contaminant removal rate, 10% lower than the well-mixed equivalent, also contributes to this increasing rate of divergence between the two predictions. Figure 23 highlights how important it is to accurately assess these major characteristics. At the end of this 1800 s exposure period an occupant in this room would be likely to see 50% more exposure to this arbitrary contaminant than the well-mixed model would predict and could see more than three times the well-mixed exposure at some locations in the breathing-zone.

During the releasing period and the mixing stage of the decaying period, when the total average concentration, $\overline{\overline{\mathcal{C}_j}}$, is the highest and the set of local concentration measurements, $\mathcal{C}_{ij}$, is the most skewed, the distribution of exposure also becomes significantly skewed. This skewness in the spatial distribution of exposure persists long after the distribution of the contaminant concentration has returned to being approximately normal. The wide range of local exposures shown in Figure 23 demonstrates the high degree of uncertainty that exists in the possible exposure an occupant could see in this room when the source location is unknown, and how widely it can differ from the well-mixed assumption, particularly exposure near the source during the release. Users of traditional well-mixed models could take this uncertainty into consideration, possibly by including safety factors to account for the spatiotemporal uncertainty within a room and ensure a desired level of protection from a particular contaminant/source of concern.

## 6 Discussion

For a majority of rooms, particularly those employing mixing ventilation strategies, the well-mixed model provides a good prediction of a room's total average concentration and occupant exposure. However, these simplified models inherently introduce additional uncertainty in the model prediction (Keil 2000). Due to the complexities of real room airflows and the resulting heterogeneity in the spatial distributions of contaminants within a room, the actual level of exposure an occupant may see can deviate from an idealized well-mixed condition in several ways. First, the room on average may be better or worse at removing contaminants from the occupied zone than a well-mixed model would predict. Second, due to variability in room parameters (e.g. source location) or uncertainty in the room airflow pattern due to variability in boundary conditions (e.g. airflow rate or room heat load), the average breathing-zone concentration in a room can vary for different instances of the same release. The application of our regression curve fitting model enabled us to assess *how* the average transient concentration within the breathing-zone tends to deviate from the well-mixed prediction in response to some set of uncertain input conditions, in this case, an uncertain source location. Finally, there is also variability in the spatial distribution of the contaminant concentration within the room for each contaminant release scenario. The methodology presented in this study enables the detailed assessment and quantification of the specific ways in which a room's occupant exposures can deviate from a well-mixed prediction, as well as quantifying the uncertainty in the range of possible local exposures in the occupied breathing-zone. These methods can be applied to quantify and evaluate the spatially resolved performance of different ventilation strategies, and other techniques for mitigating occupant exposure to airborne contaminants while considering uncertainty in different influential input parameters.

The case study presented in this paper was deliberately simple for the purposes of demonstration. We examine the impact of a single uncertain in-room parameter, the source location. And while simple, this case illustrated several key features of this proposed methodology. First, it allows a user to characterize how a room on average can deviate from the well-mixed assumption over time, given some set of uncertain room parameter(s). For example, in this room (under this flow condition) after a thirty-minute release from some unknown source location, the total average concentration in the breathing-zone is 14% higher than the well-mixed prediction. Previous studies have attempted to characterize how real rooms deviate from perfectly well-mixed rooms such as Sohn and Small (1998), which

quantified the effective air exchange rates and effective mixing volumes of real rooms under specific conditions. The curve fitting method we proposed enables a more detailed characterization of *how* a room's average concentration deviates from a well-mixed condition over time as a result of our multi-parameter curve fit. For example in this room, we determined that the room time constant and the steady-state concentrations were both higher than their corresponding well-mixed values, 11% and 18% higher respectively. Second, this methodology enables the assessment of how a room's average transient concentration may vary in response to some set of uncertain room parameter(s). For example, in this case with a single steady room airflow, the observed time constant was not impacted by changes in the source location. While conversely, the average steady-state concentration did vary significantly for different source locations. It ranged from 89% to 135% of the well-mixed steady-state concentration for the set of source locations tested with a relative standard deviation of 7.2%. Finally, the in-room spatial variability and the way this variability itself can vary in response to some uncertain room parameter(s) can also be evaluated using this methodology. For example, in this case, after a 30-minute release, the average standard deviation in the spatial distribution of contaminates was approximately 22% of the average concentration, but for the different source locations tested this ranged from 11% to 40%.

### 6.1 Evaluating more complex uncertain scenarios

The results of this example case would not necessarily be representative of the actual uncertainty in any real room, primarily because, while the source location is important, there are a myriad of other uncertain or variable room input parameters that could also influence the spatiotemporal variability in the in-room contaminant distribution. In this study, we only simulated a single airflow condition and limited our experimental space to the possible uncertain source locations within the room, $\vec{x}_j = [x_j, y_j, z_j]$. However, this methodology could be extended to consider a much more complex higher-dimensional uncertain experimental space by considering more of the CFD model's input parameters as uncertain. For example, things like the exact inlet flow condition (e.g., temperature, velocity, direction, turbulence), the distribution/magnitude of in-room heat sources, and possible arrangements of furniture/occupants are all potentially uncertain factors that could impact a room's uncertain performance. Probability distribution functions could be obtained/estimated for each of the $n$ input parameters, and the same algorithm used in this study (Deutsch and Deutsch 2012) could be applied to obtain a random sample of $m$ instances of this $n$-dimensional experimental space. The mathematics presented in this paper would be identical, but the subscript $j$ would refer to some instance of the entire space rather than simply a source location. Though the determining relationships between multiple uncertain inputs and spatiotemporal variability would require detailed covariance and sensitivity analysis.

Evaluating a higher $m$-dimensional space would also of course require a larger number of samples (i.e. curse of dimensionality) and a corresponding increase in the computational requirements for constructing these room models. This high computational cost may limit the number of situations where it is feasible to apply such detailed modeling techniques (i.e. fully resolved CFD models) to high-risk scenarios or high-value (e.g. chemical manufacturing facilities or the pentagon). However, it is important to note that the methodology we have outlined could be used to process data from any spatially resolved transient concentration model or set of experimental measurements, provided sufficient measurement density. Therefore, for high-dimensional uncertain spaces when it is not feasible to run CFD simulations for a sufficiently large sample, other lower fidelity spatially resolved models could be used (e.g., fast fluid dynamics models (Zuo and Chen 2010), or coarse gird CFD methods (Wang and Zhai 2012)). Using models with less spatial and/or multi-physics resolution models may result in a less accurate assessment than CFD models, but can still provide significantly more information about the in-room spatiotemporal variability than assuming rooms to be well-mixed. With these stochastic room surrogate models, building modelers will be able to incorporate the impact of in-room spatiotemporal variability into multi-zone assessments of the uncertain system performance to compare the relative significance of the airflow-driven variability in local occupant exposures compared to other sources of variability (e.g. source strength, decay rate, filtration rate, etc.) that are not impacted by variability in the local airflow.

## 7 Conclusions

This paper presented a method for the characterization and quantification of spatiotemporal uncertainty within a room. We use the method to estimate the spatiotemporal variability in a room's contaminant distribution and the resulting uncertainty occupant exposures when the location of a generic in-room contaminant source is unknown. The metrics we propose decompose the total spatiotemporal variability in a room into the variability in a room's transient average concentration and the variability of the concentration in space relative to that average. In the studied room, when the source location is uncertain, on

average the later variability in the possible breathing zone concentrations was approximately three times greater than the variability in the set of source average concentrations. We characterized the transient variability in source average concentrations using a regression curve-fit model to evaluate specific effects of room parameters, such as source location, on the uncertainty in an occupant's expected exposure. For example, we observed that in this small room the contaminant removal rate was not impacted by different source locations, but the average magnitude did depend greatly on where the source was located. Our introduction of an intercept term to our models of the transient averages enables the efficient characterization of the mixing stage offset and resulting uncertainty.

We also characterize the relative variability of concentration in space during the two periods studied. For example, we found that, regardless of the source location or absolute contaminant magnitude, the relative variability in the spatial distribution of contaminants quickly reaches a constant level after the brief decay-period mixing stage. This fully developed spatial variability is driven by the heterogeneity in the room's airflow distribution. Building modelers and operators can apply this method to perform similar detailed assessments of the spatiotemporal variability in contaminant concentration for different rooms of interest, and elucidate which in-room factors have the greatest influence on this variability in different exposure scenarios. This case study also highlights the importance of accurately assessing a room's total average behavior in order to accurately predict occupant exposures. We saw that relatively small errors in predicted concentrations can accumulate over time resulting in large differences in predicted levels of exposure.

## 8 Future work

The methodology for quantifying spatiotemporal variability presented in this study was a necessary first step in the development of a stochastic surrogate model for particular rooms (zones) for incorporation into multi-zone models in later works. Such a model must take into account the transiently varying spatial heterogeneity in the contaminant concentration within a room as well as its impact on occupant exposure. Here we limited our investigation to the trends in variability within a single room, under a single flow condition, and examined the variability in the transient concentration from different source locations. In future studies, we will investigate higher dimensional uncertain spaces and use the proposed methodology to perform detailed sensitivity analyses and determine which uncertain room inputs have the greatest impact on the spatiotemporal uncertainty. It will also allow users to identify how these parameters influence the transient development of the concentration distribution, i.e. which uncertain inputs influence which model parameters. The development of these models will ultimately enable the inclusion of in-room spatiotemporal uncertainty in larger-scale studies of indoor contaminant transport using multi-zone models. Stochastic models of each zone in a building could be constructed either from specific simulations/measurements of the uncertain conditions expected in some room(s) of interest. The end goal, once this methodology has been applied to characterize a wide range of rooms under various uncertain input conditions, will be to determine pseudo-empirical relationships between known or uncertain room inputs and our models characteristic *fit*-parameters that will enable the prediction of a room's uncertain behavior as well as the deviation form the well-mixed assumption that would be expected, based on some set of critical in-room parameters known to impact spatiotemporal variability. The method proposed in this paper will facilitate the identification of these parameters, and enable the characterization of their relationships to specific aspects of the room's transient behavior.

## Acknowledgements

This research was supported in parts by the U.S. Defense Threat Reduction Agency and performed under U.S. Department of Energy Contract No. DE-AC02-05CH11231. We would like to thank Dr. Ruoyou You for providing us with the experimental data used to validate our model, and would also like to thank ANSYS Inc. who provided us with the software licenses used for this study.

## Author contribution statement

All authors contributed to the study conception and design. Material preparation, data collection and analysis were performed by John Castellini. The first draft of the manuscript was written by John Castellini and all authors commented on previous versions of the manuscript. All authors read and approved the final manuscript.

## References

Abuhegazy M, Talaat K, Anderoglu O, et al. (2020). Numerical investigation of aerosol transport in a classroom with relevance to COVID-19. *Physics of Fluids*, 32: 103311.

Ai Z, Mak CM, Gao N, et al. (2020a). How suitable is tracer gas as a surrogate of exhaled droplet nuclei for studying airborne transmission in the built environment. In: Proceedings of 16th Conference of the International Society of Indoor Air Quality and Climate: Creative and Smart Solutions for Better Built Environments, Indoor Air 2020

Ai Z, Mak CM, Gao N, Niu J (2020b). Tracer gas is a suitable surrogate of exhaled droplet nuclei for studying airborne transmission in the built environment. *Building Simulation*, 13: 489–496.

ANSYS (2021). Ansys Fluent Theory Guide.

Ascione F, De Masi RF, Mastellone M, et al. (2021). The design of safe classrooms of educational buildings for facing contagions and transmission of diseases: A novel approach combining audits, calibrated energy models, building performance (BPS) and computational fluid dynamic (CFD) simulations. *Energy and Buildings*, 230: 110533.

ASHRAE (2019). ASHRAE terminology—A comprehensive glossary of terms for the built environment.

ASHRAE (2020). ANSI/ASHRAE Standard 55-2020.

Barbosa BPP, de Carvalho Lobo Brum N (2021). Ventilation mode performance against airborne respiratory infections in small office spaces: limits and rational improvements for Covid-19. *Journal of the Brazilian Society of Mechanical Sciences and Engineering*, 43: 316.

Baughman AV, Gadgil AJ, Nazaroff WW (1994). Mixing of a point source pollutant by natural convection flow within a room. *Indoor Air*, 4: 114–122.

Bhattacharyya S, Dey K, Paul AR, et al. (2020). A novel CFD analysis to minimize the spread of COVID-19 virus in hospital isolation room. *Chaos, Solitons and Fractals*, 139: 110294.

Buchan AG, Yang L, Atkinson KD (2020). Predicting airborne coronavirus inactivation by far-UVC in populated rooms using a high-fidelity coupled radiation-CFD model. *Scientific Reports*, 10: 19659.

Bueno de Mesquita PJ, Delp WW, Chan WR, et al. (2022). Control of airborne infectious disease in buildings: evidence and research priorities. *Indoor Air*, 32: e12965.

Castellini JE Jr, Faulkner CA, Zuo W, et al. (2022). Assessing the use of portable air cleaners for reducing exposure to airborne diseases in a conference room with thermal stratification. *Building and Environment*, 207: 108441.

Chen C, Liu W, Lin CH, et al. (2015). Accelerating the Lagrangian method for modeling transient particle transport in indoor environments. *Aerosol Science and Technology*, 49: 351–361.

Chitaru G, Berville C, Dogeanu A (2018). Numerical simulation and comparison of two ventilation methods for a restaurant - displacement vs mixed flow ventilation. *E3S Web of Conferences*, 32: 01012.

Deutsch JL, Deutsch CV (2012). Latin hypercube sampling with multidimensional uniformity. *Journal of Statistical Planning and Inference*, 142: 763–772.

Dias D, Tchepel O (2018). Spatial and temporal dynamics in air pollution exposure assessment. *International Journal of Environmental Research and Public Health*, 15: 558.

ElDegwy A, Sobhi M, Khalil E (2020). CFD application to improve infection control in office rooms. *ASHRAE Transactions*, 126(1): 220–228.

Faulkner CA, Castellini JE Jr, Zuo W, et al. (2022a). Investigation of HVAC operation strategies for office buildings during COVID-19 pandemic. *Building and Environment*, 207: 108519.

Faulkner CA, Castellini JE Jr, Lou Y, et al. (2022b). Tradeoffs among indoor air quality, financial costs, and $CO_2$ emissions for HVAC operation strategies to mitigate indoor virus in U.S. office buildings. *Building and Environment*, 221: 109282.

Fu L, Yang M, Niu J, et al. (2022). Transient tracer gas measurements: development and evaluation of a fast-response $SF_6$ measuring system based on quartz-enhanced photoacoustic spectroscopy. *Indoor Air*, 32: e12952.

Hang J, Li Y, Ching WH, et al. (2015). Potential airborne transmission between two isolation cubicles through a shared anteroom. *Building and Environment*, 89: 264–278.

Ho CK (2021). Modelling airborne transmission and ventilation impacts of a COVID-19 outbreak in a restaurant in Guangzhou, China. *International Journal of Computational Fluid Dynamics*, 35: 708–726.

Hou D, Katal A, Wang L (2021). Bayesian calibration of using $CO_2$ sensors to assess ventilation conditions and associated COVID-19 airborne aerosol transmission risk in schools. medRxiv, 2021.01.29.21250791.

Ivanov M, Mijorski S (2019). Assessment of transient CFD techniques for virtual thermal manikins' breathing simulations. *Environmental Processes*, 6: 241–251.

Jayaraman B, Finlayson EU, Sohn MD, et al. (2006). Tracer gas transport under mixed convection conditions in an experimental atrium: Comparison between experiments and CFD predictions. *Atmospheric Environment*, 40: 5236–5250.

Jones B, Das P, Chalabi Z, et al. (2015). Assessing uncertainty in housing stock infiltration rates and associated heat loss: English and UK case studies. *Building and Environment*, 92: 644–656.

Jones B, Sharpe P, Iddon C, et al. (2021). Modelling uncertainty in the relative risk of exposure to the SARS-CoV-2 virus by airborne aerosol transmission in well mixed indoor air. *Building and Environment*, 191: 107617.

Kanaan M (2019). CFD optimization of return air ratio and use of upper room UVGI in combined HVAC and heat recovery system. *Case Studies in Thermal Engineering*, 15: 100535.

Keil CB (2000). A tiered approach to deterministic models for indoor air exposures. *Applied Occupational and Environmental Hygiene*, 15: 145–151.

King MF, Noakes CJ, Sleigh PA, et al. (2013). Bioaerosol deposition in single and two-bed hospital rooms: A numerical and experimental study. *Building and Environment*, 59: 436–447.

Kong M, Zhang J, Wang J (2015). Air and air contaminant flows in office cubicles with and without personal ventilation: A CFD modeling and simulation study. *Building Simulation*, 8: 381–392.

Lee K, Zhang T, Jiang Z, et al. (2009). Comparison of airflow and contaminant distributions in rooms with traditional displacement ventilation and under-floor air distribution systems. *ASHARE Transactions*, 115(2): 306–321.

Li Y, Duan S, Yu IT, et al. (2005). Multi-zone modeling of probable SARS virus transmission by airflow between flats in Block E, Amoy Gardens. *Indoor Air*, 15: 96–111.

Li B, Duan R, Li J, et al. (2016). Experimental studies of thermal environment and contaminant transport in a commercial aircraft cabin with gaspers on. *Indoor Air*, 26: 806–819.

Liao CM, Chang CF, Liang HM (2005). A probabilistic transmission dynamic model to assess indoor airborne infection risks. *Risk Analysis*, 25: 1097–1107.

Lim T, Cho J, Kim BS (2010). The predictions of infection risk of indoor airborne transmission of diseases in high-rise hospitals: tracer gas simulation. *Energy and Buildings*, 42: 1172–1181.

Lu C, Xu H, Meng W, et al. (2020). A novel model for regional indoor $PM_{2.5}$ quantification with both external and internal contributions included. *Environment International*, 145: 106124.

Ma L, Zheng X, Guo Y, et al. (2022). A multi-zone spatial flow impact factor model for evaluating and layout optimization of infection risk in a Fangcang shelter hospital. *Building and Environment*, 214: 108931.

Méndez C, San José JF, Villafruela JM, et al. (2008). Optimization of a hospital room by means of CFD for more efficient ventilation. *Energy and Buildings*, 40: 849–854.

Mirzaie M, Lakzian E, Khan A, et al. (2021). COVID-19 spread in a classroom equipped with partition - A CFD approach. *Journal of Hazardous Materials*, 420: 126587.

Molina C, Jones B, Hall IP, et al. (2021). CHAARM: A model to predict uncertainties in indoor pollutant concentrations, ventilation and infiltration rates, and associated energy demand in Chilean houses. *Energy and Buildings*, 230: 110539.

Morozova N, Trias FX, Capdevila R, et al. (2020). On the feasibility of affordable high-fidelity CFD simulations for indoor environment design and control. *Building and Environment*, 184: 107144.

Qian H, Li Y, Nielsen PV, et al. (2009). Spatial distribution of infection risk of SARS transmission in a hospital ward. *Building and Environment*, 44: 1651–1658.

Ren C, Xi C, Wang J, et al. (2021). Mitigating COVID-19 infection disease transmission in indoor environment using physical barriers. *Sustainable Cities and Society*, 74: 103175.

Shi S, Chen C, Zhao B (2015). Air infiltration rate distributions of residences in Beijing. *Building and Environment*, 92: 528–537.

Shrubsole C, Ridley I, Biddulph P, et al. (2012). Indoor $PM_{2.5}$ exposure in London's domestic stock: modelling current and future exposures following energy efficient refurbishment. *Atmospheric Environment*, 62: 336–343.

Singer BC, Zhao H, Preble CV, et al. (2022). Measured influence of overhead HVAC on exposure to airborne contaminants from simulated speaking in a meeting and a classroom. *Indoor Air*, 32: e12917.

Sohn MD, Small MJ (1998). Parameter estimation of unknown air exchange rates and effective mixing volumes from tracer gas measurements for complex multi-zone indoor air models. *Building and Environment*, 34: 293–303.

Srebric J, Chen Q (2002). Simplified numerical models for complex air supply diffusers. *HVAC&R Research*, 8: 277–294.

Sun S, Li J, Han J (2021). How human thermal plume influences near-human transport of respiratory droplets and airborne particles: a review. *Environmental Chemistry Letters*, 19: 1971–1982.

Wang H, Zhai Z (2012). Application of coarse-grid computational fluid dynamics on indoor environment modeling: Optimizing the trade-off between grid resolution and simulation accuracy. *HVAC&R Research,* 18: 915–933.

WHO (2010). WHO Guidelines for Indoor Air Quality: Selected Pollutants. World Health Organization.

Yan Y, Li X, Shang Y, et al. (2017). Evaluation of airborne disease infection risks in an airliner cabin using the Lagrangian-based Wells-Riley approach. *Building and Environment*, 121: 79–92.

Yang X, Ou C, Yang H, et al. (2020). Transmission of pathogen-laden expiratory droplets in a coach bus. *Journal of Hazardous Materials*, 397: 122609.

Yin Y, Xu W, Gupta J, et al. (2009). Experimental study on displacement and mixing ventilation systems for a patient ward. *HVAC&R Research*, 15: 1175–1191.

Zhai ZJ, Zhang Z, Zhang W, et al. (2007). Evaluation of various turbulence models in predicting airflow and turbulence in enclosed environments by CFD: part 1—summary of prevalent turbulence models. *HVAC&R Research*, 13: 853–870.

Zhang Z, Chen Q (2007). Comparison of the Eulerian and Lagrangian methods for predicting particle transport in enclosed spaces. *Atmospheric Environment*, 41: 5236–5248.

Zhang Z, Zhang W, Zhai ZJ, et al. (2007). Evaluation of various turbulence models in predicting airflow and turbulence in enclosed environments by CFD: part 2—comparison with experimental data from literature. *HVAC&R Research*, 13: 871–886.

Zhu S, Srebric J, Spengler JD, et al. (2012). An advanced numerical model for the assessment of airborne transmission of influenza in bus microenvironments. *Building and Environment*, 47: 67–75.

Zuo W, Chen Q (2010). Fast and informative flow simulations in a building by using fast fluid dynamics model on graphics processing unit. *Building and Environment*, 45: 747–757.